

1 **Title:**

2 **More than a ligand: PD-L1 promotes oncolytic virus infection via a metabolic shift that**
3 **inhibits the type I interferon pathway.**

4

5 **Once sentence summary:** PD-L1 promotes oncolytic virus efficacy.

6

7 Jonathan J. Hodgins^{1,2,3*}, John Abou-Hamad^{1,4}, Ash Hagerman^{1,3}, Edward Yakubovich^{1,4},
8 Christiano Tanese de Souza¹, Marie Marotel^{1,3}, Ariel Buchler^{5,6}, Saleh Fadel^{7,8}, Maria M. Park^{1,3},
9 Claire Fong-McMaster^{2,9}, Mathieu F. Crupi¹, John C. Bell^{1,2}, Mary-Ellen Harper^{2,3,9}, Benjamin H.
10 Rotstein^{2,5,6}, Rebecca C. Auer^{1,2}, Barbara C. Vanderhyden^{1,3,4}, Luc A. Sabourin^{1,4}, Marie-Claude
11 Bourgeois-Daigneault^{10,11}, David P. Cook^{1,4}, and Michele Ardolino^{1,2,3*}

12 ¹ Cancer Therapeutics Program, Ottawa Hospital Research Institute

13 ² Department of Biochemistry, Microbiology, and Immunology, University of Ottawa

14 ³ Center for Infection, Immunity, and Inflammation, University of Ottawa

15 ⁴ Department of Cellular and Molecular Medicine, University of Ottawa

16 ⁵ Department of Chemistry and Biomolecular Sciences, University of Ottawa

17 ⁶ University of Ottawa Heart Institute

18 ⁷ The Ottawa Hospital

19 ⁸ Department of Pathology and Laboratory Medicine, University of Ottawa

20 ⁹ Ottawa Institute for Systems Biology

21 ¹⁰ Department of Microbiology, Infectious Diseases, and Immunology, University of Montreal

22 ¹¹ "Centre Hospitalier de l'Université de Montréal" Research Centre, Cancer and Immunopathology axes

23 *Corresponding authors

24 **E-mails:**

25 m.ardolino@uottawa.ca

26 jhodg098@uottawa.ca

27

28 **ABSTRACT**

29 Targeting the PD-1/PD-L1 axis has transformed the field of immune-oncology. While
30 conventional wisdom initially postulated that PD-L1 serves as the inert ligand for PD-1, an
31 emerging body of literature suggests that PD-L1 has cell-intrinsic functions in immune and cancer
32 cells. In line with these studies, here we show that engagement of PD-L1 via cellular ligands or
33 agonistic antibodies, including those used in the clinic, potently inhibits the type I interferon
34 pathway in cancer cells. Hampered type I interferon responses in PD-L1-expressing cancer cells
35 resulted in enhanced infection with oncolytic viruses in vitro and in vivo. Consistently, PD-L1
36 expression marked tumor explants from cancer patients that were best infected by oncolytic
37 viruses. Mechanistically, PD-L1 suppressed type I interferon by promoting a metabolic shift
38 characterized by enhanced glucose uptake and glycolysis rate. Lactate generated from glycolysis
39 was the key metabolite responsible for inhibiting type I interferon responses and enhancing
40 oncolytic virus infection in PD-L1-expressing cells. In addition to adding mechanistic insight into
41 PD-L1 intrinsic function and showing that PD-L1 has a broader impact on immunity and cancer
42 biology besides acting as a ligand for PD-1, our results will also help guide the numerous efforts
43 currently ongoing to combine PD-L1 antibodies with oncolytic virotherapy in clinical trials.

44 **Main Text:**

45 **INTRODUCTION**

46 Being expressed on many cell types, PD-L1 is a readily available ligand for PD-1 present on
47 immune cells in different tissues (1). The current model places PD-L1 as an agonistic ligand for
48 PD-1, whose engagement results in inhibition of T and NK cells (2). This pathway is exploited by
49 tumors as a mechanism of immune evasion, as evidenced by the success of antibodies blocking
50 PD-1/PD-L1 interactions in several cancer indications (3, 4). However, the implementation of
51 these therapies outpaced mechanistic understanding of this pathway, and many questions remain
52 open on the PD-1/PD-L1 axis, including what other possible functions of PD-L1 are.

53

54 Emerging literature suggests that PD-L1, beyond its one-dimensional role as the ligand for PD-1,
55 has cell-intrinsic signaling in cancer and immune cells (5, 6). PD-L1 signaling has been found to
56 modulate many cellular processes, including the TGF- β pathway and the epithelial-mesenchymal
57 transition (7-10), EGFR signaling (11), MAPK activation (12, 13), apoptosis (14, 15), DNA
58 damage (16-18), proliferation and metastasis (19), and even cellular metabolism (20, 21). In most
59 cases, the underlying mechanisms by which PD-L1 impacts these biological processes have not
60 been uncovered.

61

62 One pathway shown to be regulated by PD-L1 is the type I interferon (IFN) pathway (22-25). Type
63 I IFNs are a family of cytokines that induce a cellular anti-viral state via a JAK/STAT signaling
64 pathway that promotes the transcription of hundreds of interferon-stimulated genes (ISGs) (26).
65 Type I IFNs have other important roles in immunity and cell death (27), and it is in these contexts
66 that their connection with PD-L1 has been established. However, the ability of PD-L1 to control

67 viral infection, arguably the most prominent function of type I IFNs, has not been explored. When
68 investigating PD-L1 expression in cancer cells, this relationship becomes even more important in
69 light of the tremendous interest in combining PD-L1 blockade with Oncolytic Viruses (OVs).

70

71 OVs are viruses with a natural or engineered tropism for cancer cells over normal cells (28, 29),
72 as a result of deficiencies in type I IFN signaling in cancer cells arising during transformation (28,
73 29). Preclinical and clinical studies frequently combine OVs with PD-1/PD-L1 blockade, or even
74 engineer the OV to reduce PD-L1 expression in the tumor microenvironment (30, 31). However,
75 the potential for synergy or antagonism between PD-L1 blockade and OVs should be carefully
76 assessed prior to clinical translation.

77

78 To this end, we found that, by suppressing type I interferon responses, PD-L1 enhances infection
79 with OVs in vitro and in vivo. Inhibition of type I IFNs depended on a metabolic shift promoted
80 by PD-L1, resulting in enhanced rates of glucose uptake and glycolysis. Lactate generated from
81 glycolysis was key to inhibit type I IFN responses. Taken together, our data mechanistically link
82 PD-L1 cell intrinsic functions with susceptibility to OVs and provide a framework to further
83 develop combinatorial therapies that better exploit the ability of PD-L1 to promote OV efficacy in
84 cancer.

85

86 **RESULTS**

87 **PD-L1 engagement promotes oncolysis of cancer cells**

88 To test the hypothesis that PD-L1 regulates infection and oncolysis of cancer cells, we took
89 advantage of the murine prostate cancer cell line TRAMP-C2 (32), which is widely used in OV

90 preclinical studies (33-35), and constitutively expresses PD-L1 in culture (Figure S1A). To
91 generate PD-L1-deficient cells, we targeted *Cd274* (the gene coding for murine PD-L1) by
92 CRISPR/Cas9 and sorted cells lacking PD-L1 expression (Figure S1A).

93

94 To assess whether PD-L1 expression affects susceptibility to OV_s, we infected parental and
95 PD-L1-deficient TRAMP-C2 cells with the VSV Δ 51, which is highly sensitive to the anti-viral
96 effects of type I IFNs (36, 37). Strikingly, PD-L1 deletion resulted in a dramatic reduction of
97 infection and OV-induced cell death (Figures 1A-C). To confirm that PD-L1 deletion, and not an
98 experimental artefact, resulted in differences in OV infection, we complemented PD-L1 expression
99 in TRAMP-C2-*Cd274*^{-/-} cells and tested if the phenotype was rescued. As expected, PD-L1
100 complementation enhanced VSV Δ 51 infection compared to the empty vector control (Figures
101 1D-E). Increased resistance of PD-L1-deficient cells was observed not only in response to
102 VSV Δ 51, but also to vaccinia virus (Figure 1F), an oncolytic DNA virus undergoing clinical
103 testing (38), showing that PD-L1 controls OV infection and oncolysis of cancer cells.

104

105 Of the two known ligands for murine PD-L1 (6), TRAMP-C2 cells fail to express PD-1, whereas
106 CD80 was expressed by ~40% of cells in culture (Figure S1B). To determine if engagement by
107 CD80 was needed for PD-L1 to enhance OV infection, we isolated CD80⁺ or CD80⁻ cells from
108 both TRAMP-C2 or TRAMP-C2-*Cd274*^{-/-} by FACS and infected them with VSV Δ 51. In the cells
109 expressing CD80, PD-L1 enhanced viral infection (Figure 1G, left side). In stark contrast, in the
110 absence of CD80, PD-L1 failed to promote viral infection and there was no longer any difference
111 in infection between parental and PD-L1-deficient TRAMP-C2 cells (Figure 1G, right side). These
112 data suggest that PD-L1 engagement is required to drive permissiveness to viral infection.

113

114 Given the abundance of PD-1 in the tumor microenvironment, we tested if PD-1 engagement of
115 PD-L1 also resulted in an enhanced permissiveness to viral infection. Treatment with a
116 recombinant PD-1-hIgG1 Fc chimeric protein enhanced infection in parental TRAMP-C2 cells
117 compared to control-treated cells (Figure 1H), whereas PD-1-Fc treatment had no effect in
118 PD-L1-deficient tumor cells (Figure 1H). These data show that both CD80 and PD-1 binding to
119 PD-L1 promotes viral infection.

120

121 Next, we explored whether engagement of PD-L1 with antibodies promoted OV infection in
122 cancer cells, a question of particular interest when considering the use of PD-L1 antibodies in the
123 clinic. We pre-treated TRAMP-C2 with different PD-L1 antibodies characterized to prevent the
124 interaction between PD-L1 and PD-1 (clone 27C11), PD-L1 and CD80 (clone 17H9), or both
125 (clone 6E11) (39), which we reasoned may serve as agonists for PD-L1. Treatment with the two
126 antibodies mimicking PD-1 binding to PD-L1, clones 27C11 and 6E11, significantly enhanced
127 infection in parental TRAMP-C2, compared to isotype-treated, cells (Figure 1I), whereas no effect
128 was observed with the clone mimicking CD80 interactions with PD-L1 (17H9), perhaps because
129 CD80 was already present in our system. No effect was observed in PD-L1-deficient cells (Figure
130 1I). Taken together, this data confirms our hypothesis that PD-L1 engagement and signaling
131 enhances susceptibility to infection. Moreover, the fact that direct engagement of PD-L1 with
132 antibodies enhanced the susceptibility of cancer cells to infection rules out that uncharacterized
133 signaling downstream of CD80 was responsible for the observed phenotype.

134

135 **PD-L1 promotes oncolysis by inhibiting type I IFN responses**

136 Next, we set out to determine the mechanisms underlying PD-L1-driven enhancement of OV
137 infection. We ruled out that entry of VSV Δ 51 was impacted by deletion of PD-L1, as we found
138 equal levels of viral RNA at early time points (e.g., 1-3 hours post-infection, Figure S2A), and
139 both cell lines expressed similar levels of the VSV entry receptor LDL-R (Figure S2B).

140

141 As the type I IFN pathway is paramount for antiviral defence, we examined IFN responses induced
142 by VSV Δ 51 in parental and PD-L1-deficient cells. PD-L1-deficient TRAMP-C2 cells produced
143 ~2-fold more IFN- β compared to parental cells post-infection both at the protein and the transcript
144 levels (Figures 2A-B) and, accordingly, had higher transcription of antiviral ISGs (Figure 2C),
145 which was inhibited by PD-L1 re-complementation (Figure 2D and Figure S3A). PD-L1 regulated
146 type I IFNs not only in response to viral infection, but also to the TLR3 and RIG-I agonist poly(I:C)
147 (Figures S3B-C), suggesting that PD-L1 regulates the type I IFN response triggered by diverse
148 stimuli, and corroborating other reports linking PD-L1 and regulation of type I IFNs (22-25).

149

150 PD-L1 engagement by CD80 was required to inhibit IFN- β production in TRAMP-C2 cells (Figure
151 2E). Additionally, antibodies cross-linking of PD-L1 further suppressed type I IFN responses in
152 parental, but not PD-L1-deficient, TRAMP-C2 cells (Figure 2F). Taken together, these data show
153 that PD-L1 engagement strongly dampens type I interferon responses.

154

155 We next assessed whether PD-L1, in addition to inhibiting IFN production, also controlled
156 responsiveness to type I IFNs by regulating signaling downstream of their receptor. After acute
157 stimulation of TRAMP-C2 cells with IFN- β we observed dramatic differences in signaling
158 downstream of the type I IFN receptor; in particular, PD-L1 decreased the levels of STAT1 and

159 promoted STAT3 phosphorylation at Tyr705 (Figure 2G). Re-expression of PD-L1 altered almost
160 every step of the type I IFN pathway, from phosphorylation of TBK1 and IRF-3 (which together
161 control initial production of type I IFN), to STAT1 levels and STAT3 phosphorylation (Figure
162 S3D). Therefore, PD-L1 not only controls induction of type I IFNs, but also key signaling
163 molecules involved in their responses.

164

165 To implicate type I IFNs as the pathway responsible for the PD-L1-mediated promotion of
166 oncolysis, we pre-treated tumor cells for 24 hours with an antagonistic antibody against the type I
167 IFN receptor subunit IFNAR1. Antibody treatment ablated the differences in infection between
168 TRAMP-C2 and TRAMP-C2-*Cd274*^{-/-} cells (Figure 2H), suggesting that the phenotype was caused
169 by PD-L1 inhibition of the type I IFN pathway. Altogether, these data show that PD-L1
170 engagement promotes oncolysis via inhibition of type I IFN responses.

171

172 **PD-L1 poises cancer cells to be more susceptible to OVs**

173 The mechanistic link between PD-L1 promotion of OV infection and inhibition of type I IFN
174 responses prompted us to hypothesize that parental and PD-L1-deficient TRAMP-C2 cells will be
175 equally permissive to wild-type VSV infection, which, differently than VSV Δ 51, blocks
176 translation of newly synthesized type I IFNs upon infection. Surprisingly, PD-L1 still enhanced
177 WT VSV infection of parental TRAMP-C2 cells compared to PD-L1-deficient TRAMP-C2 cells
178 (Figure 3A), despite there being no detectable virus-induced type I IFN response in these cells
179 (Figure S4).

180

181 To better understand this unexpected result, we drew on literature showing that cancer cells often
182 exhibit a constitutive type I IFN response (40, 41), and hypothesized that PD-L1 inhibited
183 constitutive type I IFN responses. Indeed, TRAMP-C2 cells presented low but detectable
184 expression of type I IFN and ISG transcripts even before infection, which was more pronounced
185 in the absence of PD-L1 (Figure 3B). Using a sensitive IFN-reporter assay, we detected type I IFN
186 activity in uninfected TRAMP-C2 culture supernatant, and more in PD-L1-deficient cells (Figure
187 3C). Therefore, TRAMP-C2 cells present a constitutive type I IFN response which is exacerbated
188 by PD-L1 deletion.

189
190 The constitutive expression and regulation of type I IFNs, and the differential infection by VSV
191 WT, suggested that PD-L1 poised cancer cells to a pro-viral state by constitutively repressing the
192 type I IFN response and subsequent anti-viral ISG expression. To determine if this basal type I
193 IFN response was sufficient to drive differences in OV infection, we treated TRAMP-C2 cells with
194 actinomycin D at the time of VSV Δ 51 infection to block all cellular transcription, including
195 virus-induced production of type I IFNs. In this setting, the only source of type I IFNs comes prior
196 to infection, as part of the constitutive IFN response observed in cancer cells. Despite the absence
197 of virus-induced IFN, we still observed more VSV Δ 51 infection in TRAMP-C2 compared to
198 TRAMP-C2-*Cd274*^{-/-} cells (Figure 3D), suggesting that PD-L1 poises cancer cells to be more
199 amenable to oncolysis.

200

201 **PD-L1 promotes a metabolic shift in cancer cells resembling the Warburg effect.**

202 To better understand the mechanisms underlying inhibition of type I IFNs by PD-L1, we performed
203 RNA-sequencing on TRAMP-C2 and TRAMP-C2-*Cd274*^{-/-} cells, both before and after infection

204 with VSV Δ 51. We observed 2,690 and 5,486 differentially expressed genes in mock and infected
205 samples respectively (FDR<0.05), confirming that PD-L1 regulated cellular pathways before
206 infection (Figure S5A). To investigate the involvement of these pathways in the function of PD-L1,
207 we experimentally activated or inhibited some of them and examined oncolytic viral infection in
208 the presence and absence of PD-L1. TGF- β , EGFR and estrogen/androgen pathways were not
209 found to be involved in the ability of PD-L1 to promote OV infection in cancer cells, as the
210 phenotype was not lost upon experimental manipulation (Figures S5B-D).

211
212 Analysis of the differentially expressed genes showed that many metabolic enzymes were less
213 abundantly expressed in PD-L1-deficient cells, resulting in a decreased glycolysis gene set score
214 compared to parental TRAMP-C2 cells (Figure 4A), which was reflected in the differential
215 Hypoxia pathway activity in the PROGENy analysis (Figure S5A). We observed increased
216 expression of most glycolysis enzymes in TRAMP-C2 compared to TRAMP-C2-*Cd274*^{-/-} cells
217 (Figure S6A), suggesting regulation of glycolysis by PD-L1. In corroboration to this hypothesis,
218 we found that PD-L1-deficient cells had decreased glycolysis (Figure 4B) and increased oxidative
219 phosphorylation (OXPHOS) (Figure 4C). Both phenotypes were fully rescued by re-expression of
220 PD-L1 in TRAMP-C2-*Cd274*^{-/-} cells (Figures 4D-E). Accordingly, bioenergetic calculations (42)
221 show that PD-L1 reduced ATP production from OXPHOS while increasing ATP production from
222 glycolysis (Figures 4F-G). Many key parameters of mitochondrial respiration were reduced in
223 PD-L1-expressing cells (Figure S6B) which also had reduced mitochondrial content (Figures
224 S6C-D), without impacting mitochondrial ROS (Figure S6E). Increased glycolytic rate in parental
225 TRAMP-C2 cells were also confirmed by untargeted metabolomics. We quantified approximately
226 100 water-soluble metabolites on TRAMP-C2 and TRAMP-C2-*Cd274*^{-/-} in the absence of

227 infection (Table S1). The abundance of 52 metabolites was statistically different between parental
228 and PD-L1-deficient cells (Fig. 4H) including the glycolysis metabolites fructose-1,6-biphosphate,
229 dihydroxyacetone phosphate, and pyruvate, which are key indicators of glycolysis rates (43)
230 (Figure S6F).

231
232 Not only were PD-L1 expressing cells more glycolytically active, but they also presented enhanced
233 rate of in vitro glucose uptake (Figure 4I), which was dependent on PD-L1 engagement by CD80
234 (Figure 4J). The same phenotype was conserved in vivo, as determined in subcutaneous
235 TRAMP-C2 and TRAMP-C2-*Cd274*^{-/-} tumors established in immunodeficient NCG mice
236 subjected to PET scanning with the radiolabeled glucose analog [¹⁸F]-fluorodeoxyglucose. In this
237 model, any differences would be driven by PD-L1 activity on cancer cells, rather than
238 immune-dependent or PD-1-dependent mechanisms. Parental and PD-L1-deficient tumors grew at
239 similar rates in NCG mice. Consistent with our in vitro data, parental TRAMP-C2 tumors had
240 enhanced rates of [¹⁸F]-fluorodeoxyglucose uptake compared to PD-L1-deficient tumors (Figures
241 4K and Fig. S6G). Higher rates of glycolysis and glucose uptake, along with increased reliance on
242 glycolysis for ATP generation, are highly consistent with the Warburg effect, where cancer cells
243 preferentially use glycolysis over OXPHOS to meet bioenergetic demands and generate other
244 metabolites (44).

245

246 **PD-L1 promotes glycolysis and inhibits IFN responses in human cancer cells.**

247 If PD-L1 regulation of type I IFN is a well-conserved feature, we expect our findings to be
248 replicated in other cancer cell lines with similar features, in particular the metabolic characteristics
249 of TRAMP-C2 cells. To test this hypothesis, we made use of an RNA-seq dataset of 675 human

250 cancer cell lines (45) and scored each of those cell lines for their expression of PD-L1 (*CD274*)
251 and expression of genes in the Glycolysis gene set, which includes glycolysis and other metabolic
252 enzymes (Figure 5A). We hypothesized that in cell lines with high PD-L1 expression and high
253 score for the Glycolysis gene set, PD-L1 would promote glycolysis, inhibit type I IFN responses
254 and make tumor cells more susceptible to OVs. From this analysis, we chose two readily available
255 cell lines: the renal cell carcinoma line 786-0 and the gastric carcinoma line Hs746, both with high
256 glycolysis gene set scores, but with different levels of PD-L1. In both cell lines, we deleted PD-L1
257 using CRISPR/Cas9 (Figure S7A), and subjected parental and *CD274*^{-/-} cells to VSVΔ51 infection.
258 In both 786-0 and Hs746 cells, PD-L1 deletion made tumor cells more resistant to OV (Figure
259 5B-C), consistent with our hypothesis and the data in the TRAMP-C2 model. Furthermore, PD-L1
260 inhibited the constitutive and virus-induced interferon response, as well as signaling downstream
261 of the type I IFN receptor in both cell lines (Figure 5D-E and Figures S7B-C).

262
263 To test if the link between PD-L1 expression and glycolysis in cancer cells held true in primary
264 human samples, we took advantage of a single-cell RNA-sequencing dataset of 266 human tumors,
265 spanning 8 types of cancer (Table S2). We scored each tumor for expression of PD-L1 and genes
266 included in the glycolysis gene set. When we correlated the glycolysis score to PD-L1 expression
267 at the single cell level in these cancers (46), we observed that tumors with high expression of PD-
268 L1 had significantly higher glycolysis gene scores, in line with our hypothesis that PD-L1 drives
269 glycolytic metabolism in cancer cells (Figure 5F). Therefore, the effect of PD-L1 on OV infection,
270 type I IFN responses, and cellular metabolism is not unique to the TRAMP-C2 model and is
271 conserved in other human cancer cell types.

272

273 **PD-L1 inhibits type I IFN via lactate dynamics**

274 Metabolic alterations are now known to control inflammatory pathways, including type I IFN (47),
275 e.g., glycolytic enzymes and metabolites are key regulators of inflammatory cytokines and
276 anti-viral defenses (48-51). In line with this literature and considering our data, we reasoned that
277 PD-L1 inhibition of type I IFN responses was linked with its ability to promote glycolysis. Recent
278 research has mechanistically linked lactate to regulation of the type I IFN response (52). Lactate
279 is an important metabolite generated during Warburg metabolism, whose physiological role is now
280 beginning to be uncovered (53). Given its emerging role as a regulator of inflammatory responses,
281 we hypothesized that lactate was responsible for the ability of PD-L1 to inhibit type I IFNs and
282 promote virus infection.

283

284 In corroboration to our hypothesis, lactate was more abundantly produced in parental, over
285 PD-L1-deficient cancer cells lines (Figure 6A). To directly test the role of lactate in PD-L1-driven
286 inhibition of type I IFN responses, we pharmacologically perturbed lactate abundance prior to
287 VSV Δ 51 infection. First, to suppress lactate production, we used sodium oxamate and GNE-140:
288 two structurally distinct inhibitors of the enzymes responsible for conversion of pyruvate into
289 lactate: lactate dehydrogenases. Both inhibitors blocked the ability of PD-L1 to enhance virus
290 infection (Figures 6B-C). On the other hand, treatment with lactate increased the permissiveness
291 of PD-L1-deficient cells to OV infection, phenocopying the effect of PD-L1 (Figure 6D). Further,
292 boosting glycolysis and lactate production through treatment with the ATP synthase inhibitor
293 oligomycin also mimicked the effect of PD-L1 on VSV Δ 51 infection (Figure 6E). We observed
294 changes in susceptibility to OVs when tampering with lactate abundance not only in TRAMP-C2
295 cells (Figure 6A-E), but also in 786-0 and Hs746 cells (Figures 6F-I). Taken together, these

296 experiments highlight the key role of lactate in promoting PD-L1-driven permissiveness to OV
297 infection.

298

299 To associate the PD-L1-mediated metabolic switch with the type I IFN response, we examined
300 IFN- β induction and IFN receptor signaling following treatment with lactate. Lactate treatment
301 resulted in normalization of the type I IFN response between parental and PD-L1-deficient
302 TRAMP-C2 cells (Figures 6J-L), indicating that lactate is responsible for PD-L1-mediated
303 regulation of type I IFNs.

304

305 **PD-L1 promotes OV infection in vivo**

306 To determine if PD-L1 retains its ability to enhance OV infection in the more complex tumor
307 microenvironment, we investigated whether PD-L1 promoted cancer cell infection in vivo. We
308 established subcutaneous TRAMP-C2 or TRAMP-C2-*Cd274*^{-/-} tumors in immunodeficient NCG
309 mice and, when tumors reached ~ 750 mm³, we injected them with VSV $\Delta 51$ (expressing a
310 luciferase reporter). After 24 hours we assessed viral infection by in vivo imaging and plaque
311 assays. In corroboration of our in vitro studies, PD-L1-deficient tumors presented reduced
312 infection compared to parental tumors (Figures 7A-B), indicating that PD-L1 expression on tumor
313 cells drives increased OV infection in vivo.

314

315 We next investigated if atezolizumab, the clinically approved PD-L1 antibody used in checkpoint
316 inhibition immunotherapy, triggered PD-L1 function and enhanced OV infection. Pre-treatment of
317 the 786-0 and Hs746 cells with atezolizumab significantly enhanced OV infection compared to the

318 isotype control (Figures 7C-D); as expected, atezolizumab treatment had no impact on OV
319 infection in PD-L1-deficient cells.

320

321 Lastly, we asked if PD-L1 favoured OV infection in primary human cancer reasoning that PD-L1⁺
322 tumors should have higher rates of infection, based on the totality of the data presented thus far.
323 We obtained fresh tumor biopsies and subjected them to both *i)* ex vivo VSVΔ51-YFP infection
324 for 48 hours (Figure S8A); and *ii)* PD-L1 immunohistochemistry to determine the PD-L1 status of
325 tumors (PD-L1⁺ tumors are defined as $\geq 1\%$ of tumor/immune cells staining for PD-L1, in
326 accordance with clinical protocols) (Figure S8B). In a cohort of 21 patient tumors (Table S3),
327 PD-L1⁺ tumor explants were significantly better infected compared to PD-L1⁻ explants (Figure
328 7E). Importantly, infection did not correlate with pre-infection tumor viability (Figure S9A) nor
329 degree of biopsy necrosis (Figure S9B), suggesting that this analysis was not confounded by tissue
330 viability, which was very high in most biopsies analyzed. Tumors derived from male and female
331 patients were equally represented in terms of PD-L1 status (Figure S9C) and infection levels
332 (Figure S9D). Therefore, in a cohort of tumors of diverse origins and treatment history, PD-L1
333 marked tumors that were more likely to be infected by OVs, corroborating our results in human
334 tumors, and revealing an unappreciated role of PD-L1 as an OV infectivity biomarker.

335

336 **DISCUSSION**

337 Here, we show that PD-L1 inhibits the type I IFN response and enhances OV infection via a
338 pro-glycolytic shift in cancer cells resembling of Warburg metabolism. The requirement for
339 engagement by an extracellular binding partner strongly suggests that this function is mediated by
340 some signaling capacity of PD-L1. While the idea of PD-L1 “reverse signaling” has quickly gained

341 traction there is still a lack of data towards understanding if PD-L1 functions requires cross-linking
342 or conformational changes triggered by other proteins. Our data showing that CD80, a PD-1 fusion
343 protein or monoclonal antibodies, including those clinically used, boost PD-L1 functions add to
344 this debate suggesting that PD-L1 needs to be engaged to mediate its cell intrinsic functions.

345
346 PD-L1 has previously been shown to modulate type I IFNs with biochemically, transcriptomic and
347 bioinformatic approaches. Surprisingly, some of these early studies show that PD-L1 inhibits type
348 I IFN responses, while others showed the opposite (23-25). Overall, the mechanisms underlying
349 this context-specificity of PD-L1 function are unknown. It is possible that PD-L1 signals
350 differently depending on the cell type. What may be underpinning these signaling differences is
351 the extensive glycosylation of PD-L1, which is responsible for approximately 50% of its observed
352 molecular weight. Different cancer cell types/lines express different PD-L1 glycoforms (54), and
353 differential glycosylation influences PD-L1 interactions (55), and, potentially, its downstream
354 signaling. Our discovery that PD-L1 promotes glycolysis creates an intriguing link with PD-L1
355 glycosylation, which warrants further investigation.

356
357 Mechanistically, we found that PD-L1 regulates type I IFNs by promoting Warburg metabolism.
358 Strengthening our finding, previous work suggested a link between PD-L1 expression and
359 metabolism. For example, a correlation was found between tumor PD-L1 expression and PET
360 signal in different cancer types (56), similar to what we observed in vivo. Additionally, PD-L1
361 was shown to influence aerobic glycolysis and other metabolic pathways in cancer cells (20, 21,
362 57). The biological consequences of PD-L1-mediated metabolic shifts remain understudied,
363 particularly given the fact that PD-L1 is expressed on cells with metabolic functions, such as

364 pancreatic islet cells (*I*), warranting more work investigating the impact of metabolic regulation
365 by PD-L1. We have linked PD-L1 regulation of type I IFN to lactate produced during Warburg
366 metabolism. Lactate is no longer considered simply a waste product, and is now known to be
367 involved in the regulation of key oncogenes and tumor suppressor genes (58) as well as
368 inflammation (59), and a novel post-translational modification (lactylation) involving addition of
369 lactate to lysine and phenylalanine residues has been shown (60, 61).

370

371 Certainly, our data shed new light on the combination of PD-L1 blockade with OV. The rationale
372 behind this combination lies in the fact that OV infection leads to up-regulation of PD-L1 in many
373 tumor models (30, 35), and therefore blocking PD-L1 will unleash the full range of anti-tumor
374 immunity induced by OVs. Indeed, OVs combined with anti-PD-1/PD-L1 led to improvements in
375 tumor immune infiltrate and the activation status of immune cells (30, 62, 63). At the same time,
376 it is now reasonable to test if anti-PD-L1 triggers the ability of PD-L1 to enhance OV infection in
377 tumors, independent of its effect on anti-tumor immunity. In accordance with our in vitro and in
378 vivo data, in a small cohort of cancer patients we found that PD-L1 expression predicted
379 susceptibility to OV infection with only one PD-L1⁻ tumor well-infected ex vivo. Since PD-L1 in
380 tumors is regularly measured in clinical settings, it will be interesting to determine if this
381 relationship between PD-L1 and OV infection holds in future trials.

382

383 Lastly, from a clinical perspective, the fact that PD-L1 antibodies can trigger PD-L1 activity is
384 highly relevant. It is tempting to speculate that these novel, cell-intrinsic functions of PD-L1 are
385 being modulated in tumors of patients undergoing anti-PD-L1 therapy, and this may contribute to
386 anti-tumor efficacy (or lack thereof) of these therapeutic agents. Investigation in appropriate

387 murine models of cancer is needed to elucidate the role of cell-intrinsic PD-L1 function on
388 checkpoint blockade efficacy.

389

390 **MATERIALS AND METHODS**

391 **Cell lines**

392 Cell lines were cultured at 37°C in a humidified atmosphere containing 5% CO₂. TRAMP-C2 were
393 maintained in DMEM supplemented with 5% FBS, 5% NuSerum, 0.005 mg/mL bovine insulin,
394 10 nM dehydroisoandrosterone, 100 U/mL penicillin, 100 ug/mL streptomycin, 10 ug/mL
395 gentamicin sulfate, and 20 mM HEPES. 786-0, Hs746, HEK293T, L929-ISRE, and Vero cells
396 were maintained in DMEM supplemented with 10% FBS, 100 U/mL penicillin, 100 ug/mL
397 streptomycin, 10 ug/mL gentamicin sulfate, and 20 mM HEPES. Cells were regularly tested for
398 mycoplasma using PCR protocol adapted from (64). 786-0 and Vero cells were a gift from Dr.
399 John Bell (OHRI), Hs746 were purchased from ATCC, L929-ISRE generated by Dr. Bruce Beutler
400 (UT Southwestern) were a gift from Dr. Subash Sad (uOttawa), and HEK293T were a gift from
401 Dr. Ian Lorimer (OHRI).

402

403 **Generation of cell line variants**

404 Single-guide RNA (sgRNA) targeting exon 3 of the *Cd274* gene (sequence:
405 GTATGGCAGCAACGTCACGA) was cloned into the Cas9-expressing lentiCRISPR v2 vector
406 according to lentiCRISPR cloning protocol from the Zhang lab; lentiCRISPR v2 was a gift from
407 Feng Zhang (Addgene plasmid 52961; <http://n2t.net/addgene:52961>; RRID: Addgene_52961).
408 TRAMP-C2 were transiently transfected with plasmid, and subsequently treated with murine
409 IFN- γ (Peprotech) to up-regulate PD-L1 in all cells, except those with deletion of PD-L1. PD-L1

410 cells were isolated by FACS. To generate 786-0 and Hs746 *CD274*^{-/-}, cells were electroporated
411 with a ribonucleoprotein complex of ATTO550-labeled gRNA (IDT; sequences: UGG CUG CAC
412 UAA UUG UCU AUG UUU UAG AGC UAU GCU; AUU UAC UGU CAC GGU UCC CAG
413 UUU UAG AGC UAU GCU; AGC UAC UAU GCU GAA CCU UCG UUU UAG AGC UAU
414 GCU; UUG AAG GAC CAG CUC UCC CUG UUU UAG AGC UAU GCU) and recombinant
415 Cas9 (IDT) using protocols modified from the Alt-R CRISPR-Cas9 system (IDT), and
416 subsequently treated with human IFN- γ (Peprotech) to up-regulate PD-L1 in all cells except those
417 with deletion of PD-L1. PD-L1⁻ cells were isolated by FACS.

418
419 To stably express PD-L1 or control vector in TRAMP-C2-*Cd274*^{-/-}, the cDNA encoding full-length
420 murine PD-L1 was cloned into the retroviral vector pQCXIN-IRES-Thy1.1, and the resulting
421 pQCXIN-PD-L1-IRES-Thy1.1 plasmid was transfected into HEK293T cells along with
422 pCMV-VSV-G (a gift from Bob Weinberg; Addgene plasmid 8454; <http://n2t.net/addgene:8454>;
423 RRID:Addgene_8454) and pCL-Eco (a gift from Inder Verma; Addgene plasmid 12371;
424 <http://n2t.net/addgene:12371>; RRID:Addgene_12371) to generate retrovirus.
425 TRAMP-C2-*Cd274*^{-/-} were infected with this retrovirus (or retrovirus encoding
426 pQCXIN-IRES-Thy1.1 as empty vector control) supplemented with 8 μ g/mL polybrene. Cells
427 staining positively for PD-L1 and Thy1.1 (or Thy1.1 only for empty vector control) were isolated
428 by FACS.

429

430 **Oncolytic virus production and infection**

431 VSV Δ 51-YFP, VSV WT, VSV Δ 51-firefly luciferase, and vaccinia virus were gifts from Dr. John
432 Bell (OHRI). The original virus stock was propagated on Vero cells (at MOI 0.01) and cell

433 supernatant isolated 16-20 hours later for concentration of virus by high-speed centrifugation. All
434 subsequent virus stocks were generated from the original stock to avoid genetic drift. VSV Δ 51
435 titers were quantified by plaque assay using methods previously described (65).

436

437 TRAMP-C2, 786-0, and Hs746 were infected with VSV Δ 51-YFP or VSV WT by first removing
438 and washing out culture media with PBS and adding low volume of virus diluted in cold DMEM
439 to MOIs ranging from 0.001 to 100. After incubation at 37°C + 5% CO₂, supplemented growth
440 media was added.

441

442 Alternatively, TRAMP-C2 were infected with GFP-expressing B19R⁻ vaccinia virus (Copenhagen
443 strain) at MOI 0.1 for 48 hours.

444

445 **In vitro treatments**

446 Cells were treated with the following reagents, at concentrations and times indicated in figure
447 legends: recombinant murine IFN- β (PBL Assay Sciences), poly(I:C) (Invivogen), actinomycin D
448 (Sigma), recombinant mouse PD-1-Fc chimeric protein (R&D Systems) or human IgG1 control
449 (R&D Systems), afatinib (Selleck Chemicals), SB431542 (Selleck Chemicals), estradiol/E2
450 (Sigma), dihydrotestosterone/DHT (Sigma), sodium oxamate (Selleck Chemicals), (R)-GNE-140
451 (Selleck Chemicals), sodium lactate (Sigma), or oligomycin A (Selleck Chemicals).

452

453 **Coomassie staining**

454 Culture media was removed and washed out with PBS, and cells were fixed with 3:1
455 methanol:acetic acid solution for 1-3 hours. Cells were then rinsed in tap water and stained with
456 Coomassie Blue solution for 30 minutes and rinsed with tap water to remove excess dye.

457

458 **Flow cytometry**

459 Cells were briefly trypsinized, washed, and resuspended in PBS for staining. The cell suspension
460 was stained with Zombie NIR Fixable Viability Dye or Zombie Aqua Fixable Viability Dye
461 (BioLegend) to label dead cells, followed by incubation with rat anti-mouse CD16/CD32 (clone
462 2.4G2, BD Biosciences) to block Fc γ RII/III receptors. Cells were then washed and incubated with
463 fluorescently labeled antibodies. Cells were washed and resuspended in PBS and analyzed using
464 an LSRFortessa (BD Biosciences) or Celesta (BD Biosciences), or isolated using MoFlo XDP
465 (Beckman Coulter) or MA900 (SONY). Data were analyzed using FlowJo (Tree Star Inc.).

466

467 For experiment with murine cells, the following antibodies were used: BV421-anti-PD-L1 (BD,
468 clone MIH5), PE-Cy5-anti-CD80 (BioLegend, clone 16-10A1), PE-Cy7-anti-PD-1 (BioLegend,
469 clone 29F.1A12), PE-anti-LDLR (R&D Systems, clone 263123). For experiments with human
470 cells, BV421-anti-PD-L1 (BD, clone MIH1) was used.

471

472 **RNA isolation, cDNA synthesis, and qPCR**

473 RNA was isolated using GenElute RNA Miniprep Kit (Sigma) as per manufacturer's protocol.
474 cDNA was synthesized using iScript Reverse Transcription Supermix (Bio-Rad) as per
475 manufacturer's protocol. qPCR was run using iTaq Universal SYBR Green Supermix (Bio-Rad),

476 using primers listed in the table below. qPCR data normalized to murine *Gapdh* gene or human
 477 *18S* gene using the $2^{-\Delta\Delta C_t}$ method.

VSV N	Forward	GAT AGT ACC GGA GGA TTG ACG ACT A
	Reverse	TCA AAC CAT CCG AGC CAT TC
<i>Ifnb1</i>	Forward	CGC TGC GTT CCT GCT GTG
	Reverse	GAT CTT GAA GTC CGC CCT GTA G
<i>Mx1</i>	Forward	GAC CAT AGG GGT CTT GAC CAA
	Reverse	AGA CTT GCT CTT TCT GAA AAG CC
<i>Oas1b</i>	Forward	TTC TAC GCC AAT CTC ATC AGT G
	Reverse	GGT CCC CCA GCT TCT CCT TAC
<i>Eif2ak</i>	Forward	ATG CAC GGA GTA GCC ATT ACG
	Reverse	TGA CAA TCC ACC TTG TTT TCG T
<i>Isg15</i>	Forward	TGA CGC AGA CTG TAG ACA CG
	Reverse	TGG GGC TTT AGG CCA TAC TC
<i>Gapdh</i>	Forward	CAT CAC CAT CTT CCA GGA GCG
	Reverse	GAG GGG CCA TCC ACA GTC TTC
<i>MT-ND1</i>	Forward	AACATACCCATGGCCAACCT
	Reverse	AGCGAAGGGTTGTAGTAGCCC
<i>IFNB1</i>	Forward	TCCAAATTGCTCTCCTGTTG
	Reverse	GCAGTATTCAAGCCTCCCAT
<i>MX1</i>	Forward	CTGCGAGGAGATCGGTTCTG
	Reverse	CTGCACCTCCTTGAATGGT
<i>18S</i>	Forward	GTAACCCGTTGAACCCCAT

	Reverse	CCATCCAATCGGTAGTAGCG
--	---------	----------------------

478

479 **ELISA**

480 IFN- β was analyzed in culture supernatant following VSV Δ 51-YFP/VSV WT infection or
481 transfection with poly(I:C) (Invivogen), using Mouse IFN- β Quantikine ELISA Kit (R&D
482 Systems), as per manufacturer's instructions.

483

484 **Western blotting**

485 Following infection or treatment with recombinant murine IFN- β (PBL Assay Sciences), cells
486 were lysed in RIPA supplemented with cOmplete protease inhibitor cocktail (Roche) and
487 PhosSTOP phosphatase inhibitor cocktail (Roche). Protein concentration was quantified by BCA
488 Assay using MicroBCA Protein Assay Kit (ThermoFisher), and samples were denatured in
489 Laemmli buffer (Bio-Rad) supplemented with 5% β -mercaptoethanol. Proteins were separated on
490 8-12% polyacrylamide (acrylamide/bis-acrylamide 37.5:1, Bio-Rad) gel at 60 mA, and transferred
491 to a PVDF membrane for 90 minutes at 100V. Membranes were probed with the following primary
492 antibodies diluted in 5% w/v BSA in 1X TBS + 0.1% Tween20: anti-pIRF3 S396 (CST), anti-IRF3
493 (CST), anti-pTBK1 S172 (CST), anti-TBK1 (CST), anti-pSTAT1 Y701 (CST), anti-STAT1
494 (CST), anti-pSTAT3 Y705 (CST), anti-STAT3 (CST), anti-PD-L1 (Abcam), anti-PD-1 (CST),
495 and anti- β -actin (CST). Membranes were further probed with appropriate species-specific
496 HRP-conjugated secondary antibodies (CST) and developed using ECL reagent (Bio-Rad).

497

498 **In vitro antibody treatment**

499 Anti-IFNAR1 (clone MAR1-5A3) was purchased from Leinco. PD-L1 monoclonal antibody
500 clones 6E11, 17H9, and 27C11 were gifts from Dr. Ira Mellman (Genentech). Tecentriq®
501 (atezolizumab) was purchased from The Ottawa Hospital Pharmacy department. TRAMP-C2,
502 786-0, or Hs746 cells were pre-treated with these antibodies or appropriate isotype controls
503 (Leinco) for 24 hours prior to further manipulation/analysis at concentrations indicated in figure
504 legends.

505

506 **Type I interferon reporter assay**

507 100 µL of cell culture supernatant was isolated from cultured cells and placed on adherent
508 L929-ISRE cells (expressing luciferase under the control of a type I interferon sensitive ISRE
509 promoter) for 4-6 hours. Luciferase expression was assessed using Luciferase Assay System
510 (Promega) and luminescence measured on plate reader (BioTek).

511

512 **RNA-seq sample preparation**

513 RNA was collected as described above from mock-infected TRAMP-C2 cells and
514 TRAMP-C2-*Cd274*^{-/-} or those same cells infected with VSVΔ51-YFP at MOI 0.1 for 8 hours.

515

516 **RNA-seq library preparation and sequencing**

517 Total RNA was quantified using a NanoDrop Spectrophotometer ND-1000 (NanoDrop
518 Technologies, Inc.) and its integrity was assessed on a 2100 Bioanalyzer (Agilent Technologies).
519 Libraries were generated from 250 ng of total RNA as follows: mRNA enrichment was performed
520 using the NEBNext Poly(A) Magnetic Isolation Module (New England BioLabs). cDNA synthesis
521 was performed using the NEBNext RNA First Strand Synthesis and NEBNext Ultra Directional

522 RNA Second Strand Synthesis Modules (New England BioLabs). The remaining steps of library
523 preparation were done using the NEBNext Ultra II DNA Library Prep Kit for Illumina (New
524 England BioLabs). Adapters and PCR primers were purchased from New England BioLabs.
525 Libraries were quantified using the Quant-iT™ PicoGreen® dsDNA Assay Kit (Life Technologies)
526 and the Kapa Illumina GA with Revised Primers-SYBR Fast Universal kit (Kapa Biosystems).
527 Average size fragment was determined using a LabChip GX (PerkinElmer) instrument. Libraries
528 were then sequenced on a NovaSeq6000 S4 200 cycle (2 x 100bp) flow cell to an approximate
529 depth of 30M reads per sample.

530

531 **RNA-seq processing and differential expression**

532 Transcript quantification for each sample was performed using Kallisto (v0.45.0) (66) with the
533 GRCm38 transcriptome reference and the -b 50 bootstrap option. The R package Sleuth (v0.30.0)
534 (67) was then used to construct general linear models for the log-transformed expression of each
535 gene across experimental conditions. Wald's test was used to test for differential expression
536 between groups and the resultant *p*-values were adjusted to *q*-values using the
537 Benjamini-Hochberg false discovery rate method.

538

539 **Signalling inference and gene set scoring**

540 Relative activities of 14 signalling pathways were inferred using the R package PROGENy
541 (v.1.9.6) (68), which provides a prebuilt regression model for signalling activity based on
542 consistently responsive genes. Single-sample gene set scoring was performed using the R package
543 singscore (v1.17.) (69), which computes independent scores for each sample from rank-based
544 statics for each gene in the set.

545

546 **MitoTracker/MitoSOX**

547 TRAMP-C2 cells were briefly trypsinized and re-suspended in PBS. Cells were counted and
548 500,000 cells were stained with 500 nM MitoTracker Deep Red FM (ThermoFisher) and 10 μ M
549 MitoSOX Red Mitochondrial Superoxide Indicator (ThermoFisher) for 10 minutes at 37°C. Dye
550 was washed out with PBS and cells were analyzed by flow cytometry within 1 hour.

551

552 **Mitochondrial DNA and nuclear DNA quantification**

553 Mitochondrial DNA and nuclear DNA were isolated using organic solvent extraction-based
554 protocol adapted from (70). qPCR performed as described above using primers amplifying
555 MT-ND1 (for mitochondrial DNA) and 18S rRNA (for nuclear DNA).

556

557 **Seahorse extracellular flux analysis**

558 20,000 TRAMP-C2 cells/well were seeded into 96-well Seahorse plate one day prior to the
559 Seahorse assay. On the day of the assay, cells were equilibrated for one hour in DMEM
560 supplemented with 4 mM glutamine, 1 mM sodium pyruvate, 25 mM glucose, at pH 7.4. Oxygen
561 consumption rate (OCR) and extracellular acidification rate (ECAR) were measured by monitoring
562 dissolved oxygen and pH using the XF96 extracellular flux analyzer (Seahorse Bioscience) above
563 the cell monolayer under basal conditions and following treatment with oligomycin (1 μ M), FCCP
564 (0.5 μ M), and rotenone + antimycin A (1 μ M each).

565

566 **Glucose uptake**

567 In vitro glucose uptake was measured following 10 minutes of uptake using the Glucose
568 Uptake-Glo Assay kit (Promega), as per manufacturer's instructions.

569

570 **Metabolomics**

571 Levels of metabolites from TRAMP-C2 cells and culture media following 48 hours of culture were
572 quantified by liquid chromatography mass spectrometry (LC-MS). Sample temperature was
573 maintained on ice or dry ice where possible, and all solvents were MS grade and pre-equilibrated
574 to -20°C.

575

576 Cell pellets and media/supernatant were collected to a pre-chilled 2 mL tube containing 6 washed
577 ceramic beads (1.4 mm) and 230 μ l of methanol:water (1:1). Samples were vortexed 10s and cell
578 lysis was done by beating for 60 s at 2000 rpm (bead beating was done twice) after adding 220 μ L
579 of acetonitrile. Samples were then incubated with a 2:1 dichloromethane:water solution on ice for
580 10 minutes. The polar and non-polar phases were separated by centrifugation at 4000g for 10
581 minutes at 1°C. The upper polar phase was dried using a refrigerated CentriVap Vacuum
582 Concentrator at -4°C (LabConco Corporation, Kansas City, MO). Samples were resuspended in
583 water and run on an Agilent 6470A tandem quadruple mass spectrometer equipped with a 1290
584 Infinity II ultra-high-performance LC (Agilent Technologies) using the Metabolomics Dynamic
585 MRM Database and Method (Agilent), which uses an ion-pairing reverse phase chromatography.
586 This method was further optimized for phosphate-containing metabolites with the addition of
587 5 μ M InfinityLab deactivator (Agilent) to mobile phases A and B, which requires decreasing the
588 backflush acetonitrile to 90%. Multiple reaction monitoring (MRM) transitions were optimized
589 using authentic standards and quality control samples. Metabolites were quantified by integrating

590 the area under the curve of each compound using external standard calibration curves with Mass
591 Hunter Quant (Agilent). No corrections for ion suppression or enhancement were performed, as
592 such, uncorrected metabolite concentrations are presented.

593

594 **Enzymatic measurement of L-lactate**

595 L-lactate was quantified in culture supernatant using colorimetric assay (Abcam), as per
596 manufacturer's protocol.

597

598 **Mice and tumor injection**

599 NCG mice (NOD-*Prkdc*^{em26Cd52}*Il2rg*^{em26Cd22}/NjuCr1, lacking functional T, B, and NK cells) were
600 purchased from Charles River Laboratory and maintained at the University of Ottawa. For all
601 experiments, male mice were used to match the male origin of injected prostate cancer cell lines
602 (TRAMP-C2). To generate subcutaneous tumors, 1-2*10⁶ cancer cells were resuspended in
603 Matrigel (BD Biosciences) and injected in the left flank.

604

605 **In vivo VSVΔ51 infection and bioluminescence imaging**

606 For in vivo treatments of NCG mice with VSVΔ51-firefly luciferase, subcutaneous TRAMP-C2
607 tumors were injected for 24 hours with 10⁸ PFU of virus by intra-tumoral injection of 100 μL of a
608 10⁹ PFU/mL solution in sterile PBS. Mice were injected when tumors reached 750 mm³.

609

610 24 hours post-infection with VSVΔ51-firefly luciferase, tumor-bearing mice were subjected to
611 IVIS imaging. Mice were injected intraperitoneally with D-luciferin (Perkin Elmer) at a dose of

612 150 mg/kg for 15 minutes prior to isoflurane anesthesia. Mice were imaged using an IVIS
613 Spectrum (Perkin Elmer). Investigators were not blinded during imaging.

614

615 **Ex vivo virion quantification of infected mouse tumors**

616 Tumors were resected, weighed, and flash frozen in dry ice. Later, tumors were mechanically lysed
617 using a TissueLyser II (Qiagen), in PBS supplemented with cOmplete protease inhibitor cocktail
618 (Roche), using glass beads. Cell debris removed via centrifugation and 70 μ m filters, and
619 supernatant serially diluted for plaque assay as described above. Titers reported in PFU/mg of
620 tumor.

621

622 **[¹⁸F]-FDG PET**

623 Tumor-bearing mice (tumor diameter 750 mm³, n = 5-6 per group) fasted 5-8 hours before the
624 imaging session were anesthetized with 2% isoflurane and intravenously injected with [¹⁸F]-FDG
625 (5.98 ± 1.92 MBq) as a bolus over 30 sec via the lateral tail vein. Mice remained under isoflurane
626 anesthesia in an induction chamber and body temperature was maintained with a heat lamp. Blood
627 glucose measurements (mM) were taken via tail vein blood sampling before and after the PET
628 scan using a MediSure Blood Glucose Monitoring System. 40 minutes after radiotracer delivery,
629 mice were positioned in the PET scanner and a 10 min transmission scan was performed. A
630 whole-body static scan was immediately acquired between 50-60 min using a Siemens DPET
631 scanner. Emission data were corrected for attenuation and scatter, then reconstructed using the
632 3D-OSEM/MAP algorithm. Volumetric regions of interest (ROIs) were drawn conforming to
633 tumor margins and quantified using a threshold of 25% of SUVmax (SUV₂₅) (Savaikar et al.,

634 2020). Uptake values obtained in $\text{Bq}\cdot\text{cc}^{-1}$ were converted to SUV using the injected dose (Bq) and
635 animal body weight (kg).

636

637 **Bioinformatic analyses of human cell line RNA-seq**

638 Analysis of expression levels of *CD274* transcript and HALLMARK_GLYCOLYSIS gene
639 module (71, 72) in cell lines was performed using information from the RNA-Seq dataset
640 E-MTAB-2706, which contains genome-wide transcriptome profiles of 675 cancer cell lines.
641 Briefly, we downloaded the Reads Per Kilobase of transcript, per Million (RPKM) file containing
642 all sequencing reads for each cell line, along with a file containing the gene names in various
643 formats and a metadata file describing the samples. We then converted gene IDs in the expression
644 matrix to gene symbols and removed duplicates and missing values. We next added sample names
645 to the columns of the expression matrix, before leveraging the R-based package singscore (69) that
646 allows for rank-based statistics to score a sample's gene expression profile according to the
647 activities of genes provided by curated gene modules. We set a cut-off on each axis at the mean of
648 each value plus two standard deviations.

649

650 **Malignant cell PD-L1 expression and gene set activity**

651 We have previously compiled and processed a collection of scRNA-seq data from 266 epithelial
652 tumours (46). Automated annotation of cell types had been performed in conjunction with a copy
653 number alteration inference to identify the malignant population of each data set. Only tumours
654 with >200 malignant cells were retained in the cohort. Average PD-L1 expression
655 (log-transformed counts per 10k transcripts) was calculated from this fraction. Gene set scores for
656 the MSigDB Hallmark Hypoxia and Glycolysis gene sets were calculated for individual cells using

657 the R package UCell, which implements a rank-based signature scoring method based on the
658 Mann-Whitney U statistic.

659

660 **Immunohistochemistry**

661 Fresh tumor biopsies were fixed in 10% neutral-buffered formalin for 24 hours prior to
662 paraffin-embedding and sectioning. Sections were rehydrated using xylene and ethanol and
663 subjected to antigen retrieval using 10 mM citrate buffer (pH 6.0) in a pressure cooker for 10
664 minutes. Sections were blocked in 10% normal goat serum (BioLynx) and incubated with
665 anti-PD-L1 (clone 28-8, Abcam) overnight at 4°C. Endogenous peroxidase activity was quenched
666 using 3% hydrogen peroxide and incubated with HRP-conjugated goat anti-rabbit (Cell Signaling
667 Technologies). Detection performed using DAB Substrate (Vector Laboratories), followed by
668 hematoxylin counterstaining. Sections were dehydrated and stabilized with mounting medium
669 (ThermoFisher). PD-L1 expression was scored by a blinded trained pathologist. The percentage of
670 tumor cells that stained with the PD-L1 antibody was estimated on each slide. The average
671 intensity of staining was scored as 0 (no staining), 1+ (weak intensity), 2+ (moderate intensity),
672 and 3+ (strong intensity). The cellular compartment with positive staining was noted; this included
673 nuclear, cytoplasmic, or membranous. The background inflammatory cells were examined for
674 positive staining as well, and percentage of necrotic cells.

675

676 **Ex vivo infection of patient tumors**

677 Fresh tumor biopsies were cut into 2 x 2 x 2 cm cores using a biopsy punch and scalpel. Each
678 tumor core placed into individual wells of 24-well plate with DMEM supplemented with 10%
679 FBS, 100 U/mL penicillin, 100 ug/mL streptomycin, 10 ug/mL gentamicin sulfate, and 20 mM

680 HEPES. Cores were infected in quadruplicate with MOI 100, 30, 3, 1, or 0.1 of VSV Δ 51-YFP
681 (assuming $\sim 1 \times 10^6$ cells per core) or uninfected control. Concurrently, tumor cores analyzed by
682 alamarBlue Assay (ThermoFisher) as per manufacturer's protocol. Tumors were infected for 48
683 hours prior to imaging YFP reporter from the virus using EVOS Imaging System (ThermoFisher).
684 Virus infection was quantified by quantifying percentage of tumor area that is YFP⁺, using ImageJ
685 (in a blinded fashion). The only exclusion criteria for a tumor in this study was lack of viability
686 based on alamarBlue results.

687

688 **Statistical analyses**

689 All in vitro experiments repeated at least 3 times, unless otherwise stated. Mouse studies were
690 performed twice, unless otherwise stated. Statistical analyses were performed using GraphPad
691 Prism (GraphPad). Experiments with two independent conditions were analysed by two-tailed
692 unpaired Student's t test, one-way ANOVA to compare three or more conditions, and two-way
693 ANOVA (with Sidak's correction for multiple comparisons) to compare groups influenced by two
694 variables. Differences between experimental groups were considered significant when $p < 0.05$.

695

696 **Study approvals**

697 Mouse studies were reviewed and approved by Animal Care and Veterinary Services at the
698 University of Ottawa in accordance with the guidelines of the Canadian Institutes of Health
699 Research. For human studies, informed and written consent in accordance with the Declaration of
700 Helsinki was obtained from all patients, and approval was obtained from The Ottawa Hospital
701 (REB 20180221-02H).

702

703 **LIST OF SUPPLEMENTARY MATERILAS**

704 Figure S1 to S9

705

706 **References**

- 707 1. M. E. Keir *et al.*, Tissue expression of PD-L1 mediates peripheral T cell tolerance. *J Exp*
708 *Med* **203**, 883-895 (2006).
- 709 2. N. Patsoukis, Q. Wang, L. Strauss, V. A. Boussiotis, Revisiting the PD-1 pathway.
710 *Science Advances* **6**, eabd2712 (2020).
- 711 3. B. Homet Moreno, A. Ribas, Anti-programmed cell death protein-1/ligand-1 therapy in
712 different cancers. *Br J Cancer* **112**, 1421-1427 (2015).
- 713 4. A. Ribas, J. D. Wolchok, Cancer immunotherapy using checkpoint blockade. *Science*
714 **359**, 1350-1355 (2018).
- 715 5. E. D. Lucas *et al.*, PD-L1 Reverse Signaling in Dermal Dendritic Cells Promotes
716 Dendritic Cell Migration Required for Skin Immunity. *Cell Rep* **33**, 108258 (2020).
- 717 6. A. V. R. Kornepati, R. K. Vadlamudi, T. J. Curiel, Programmed death ligand 1 signals in
718 cancer cells. *Nat Rev Cancer* **22**, 174-189 (2022).
- 719 7. R. Saleh, R. Z. Taha, V. Sasidharan Nair, N. M. Alajez, E. Elkord, PD-L1 Blockade by
720 Atezolizumab Downregulates Signaling Pathways Associated with Tumor Growth,
721 Metastasis, and Hypoxia in Human Triple Negative Breast Cancer. *Cancers (Basel)* **11**,
722 (2019).
- 723 8. J. Chen *et al.*, STAT1/IFIT2 signaling pathway is involved in PD-L1-mediated epithelial-
724 to-mesenchymal transition in human esophageal cancer. *Clin Transl Oncol* **24**, 927-940
725 (2022).
- 726 9. M. J. Chen *et al.*, PD-L1 expressed from tumor cells promotes tumor growth and invasion
727 in lung cancer via modulating TGF- β 1/SMAD4 expression. *Thorac Cancer* **13**, 1322-
728 1332 (2022).
- 729 10. Y. Wang *et al.*, PD-L1 induces epithelial-to-mesenchymal transition via activating
730 SREBP-1c in renal cell carcinoma. *Med Oncol* **32**, 212 (2015).
- 731 11. T. Li *et al.*, Exploring a Tumor-Intrinsic PD-L1 Signal with Proximity-Dependent Biotin
732 Identification in Lung Cancer Cells. *Biochemistry* **58**, 2293-2296 (2019).
- 733 12. C. Chen *et al.*, PD-L1 tumor-intrinsic signaling and its therapeutic implication in triple-
734 negative breast cancer. *JCI Insight* **6**, (2021).
- 735 13. M. Passariello *et al.*, Novel Human Anti-PD-L1 mAbs Inhibit Immune-Independent
736 Tumor Cell Growth and PD-L1 Associated Intracellular Signalling. *Sci Rep* **9**, 13125
737 (2019).
- 738 14. H. Ghebeh *et al.*, Doxorubicin downregulates cell surface B7-H1 expression and
739 upregulates its nuclear expression in breast cancer cells: role of B7-H1 as an anti-
740 apoptotic molecule. *Breast Cancer Res* **12**, R48 (2010).
- 741 15. T. Kong *et al.*, CD44 Promotes PD-L1 Expression and Its Tumor-Intrinsic Function in
742 Breast and Lung Cancers. *Cancer Res* **80**, 444-457 (2020).

- 743 16. X. Tu *et al.*, PD-L1 (B7-H1) Competes with the RNA Exosome to Regulate the DNA
744 Damage Response and Can Be Targeted to Sensitize to Radiation or Chemotherapy. *Mol*
745 *Cell* **74**, 1215-1226.e1214 (2019).
- 746 17. J. Yu *et al.*, Regulation of sister chromatid cohesion by nuclear PD-L1. *Cell Research* **30**,
747 590-601 (2020).
- 748 18. S. De, E. G. Holvey-Bates, K. Mahen, B. Willard, G. R. Stark, The ubiquitin E3 ligase
749 FBXO22 degrades PD-L1 and sensitizes cancer cells to DNA damage. *Proc Natl Acad*
750 *Sci U S A* **118**, (2021).
- 751 19. C. A. Clark *et al.*, Tumor-Intrinsic PD-L1 Signals Regulate Cell Growth, Pathogenesis,
752 and Autophagy in Ovarian Cancer and Melanoma. *Cancer Res* **76**, 6964-6974 (2016).
- 753 20. C. H. Chang *et al.*, Metabolic Competition in the Tumor Microenvironment Is a Driver of
754 Cancer Progression. *Cell* **162**, 1229-1241 (2015).
- 755 21. M. Garige *et al.*, PD-L1 Mediates IFN γ -Regulation of Glucose but Not of Tryptophan
756 Metabolism in Clear Cell Renal Cell Carcinoma. *Frontiers in oncology* **12**, 858379
757 (2022).
- 758 22. M. Gato-Canas *et al.*, PDL1 Signals through Conserved Sequence Motifs to Overcome
759 Interferon-Mediated Cytotoxicity. *Cell Rep* **20**, 1818-1829 (2017).
- 760 23. B. Diskin *et al.*, PD-L1 engagement on T cells promotes self-tolerance and suppression of
761 neighboring macrophages and effector T cells in cancer. *Nat Immunol* **21**, 442-454
762 (2020).
- 763 24. Y. Gao *et al.*, Acetylation-dependent regulation of PD-L1 nuclear translocation dictates
764 the efficacy of anti-PD-1 immunotherapy. *Nat Cell Biol* **22**, 1064-1075 (2020).
- 765 25. H. Cheon, E. G. Holvey-Bates, D. J. McGrail, G. R. Stark, PD-L1 sustains chronic,
766 cancer cell's intrinsic responses to type I interferon, enhancing resistance to DNA
767 damage. *Proceedings of the National Academy of Sciences* **118**, e2112258118 (2021).
- 768 26. F. McNab, K. Mayer-Barber, A. Sher, A. Wack, A. O'Garra, Type I interferons in
769 infectious disease. *Nat Rev Immunol* **15**, 87-103 (2015).
- 770 27. L. Zitvogel, L. Galluzzi, O. Kepp, M. J. Smyth, G. Kroemer, Type I interferons in
771 anticancer immunity. *Nat Rev Immunol* **15**, 405-414 (2015).
- 772 28. B. D. Lichty, C. J. Breitbach, D. F. Stojdl, J. C. Bell, Going viral with cancer
773 immunotherapy. *Nat Rev Cancer* **14**, 559-567 (2014).
- 774 29. K. Geoffroy, M. C. Bourgeois-Daigneault, The pros and cons of interferons for oncolytic
775 virotherapy. *Cytokine Growth Factor Rev* **56**, 49-58 (2020).
- 776 30. D. Zamarin *et al.*, PD-L1 in tumor microenvironment mediates resistance to oncolytic
777 immunotherapy. *J Clin Invest* **128**, 1413-1428 (2018).
- 778 31. M. E. Wedge *et al.*, Virally programmed extracellular vesicles sensitize cancer cells to
779 oncolytic virus and small molecule therapy. *Nat Commun* **13**, 1898 (2022).
- 780 32. B. A. Foster, J. R. Gingrich, E. D. Kwon, C. Madias, N. M. Greenberg, Characterization
781 of prostatic epithelial cell lines derived from transgenic adenocarcinoma of the mouse
782 prostate (TRAMP) model. *Cancer Res* **57**, 3325-3330. (1997).
- 783 33. S. Varghese *et al.*, Enhanced therapeutic efficacy of IL-12, but not GM-CSF, expressing
784 oncolytic herpes simplex virus for transgenic mouse derived prostate cancers. *Cancer*
785 *Gene Ther* **13**, 253-265 (2006).
- 786 34. M. J. Atherton *et al.*, Transforming the prostatic tumor microenvironment with oncolytic
787 virotherapy. *Oncoimmunology* **7**, e1445459 (2018).

- 788 35. N. E. Annels *et al.*, Oncolytic Reovirus-Mediated Recruitment of Early Innate Immune
789 Responses Reverses Immunotherapy Resistance in Prostate Tumors. *Mol Ther Oncolytics*
790 **20**, 434-446 (2021).
- 791 36. D. F. Stojdl *et al.*, VSV strains with defects in their ability to shutdown innate immunity
792 are potent systemic anti-cancer agents. *Cancer Cell* **4**, 263-275 (2003).
- 793 37. E. Hastie, V. Z. Grdzlishvili, Vesicular stomatitis virus as a flexible platform for
794 oncolytic virotherapy against cancer. *The Journal of general virology* **93**, 2529-2545
795 (2012).
- 796 38. M. C. M. B. *et al.*, A phase I/II study of Pexa-Vec oncolytic virus in combination with
797 immune checkpoint inhibition in refractory colorectal cancer. *Journal of Clinical*
798 *Oncology* **38**, 117-117 (2020).
- 799 39. S. A. Oh *et al.*, PD-L1 expression by dendritic cells is a key regulator of T-cell immunity
800 in cancer. *Nature Cancer* **1**, 681-691 (2020).
- 801 40. T. Taniguchi, A. Takaoka, A weak signal for strong responses: interferon-alpha/beta
802 revisited. *Nat Rev Mol Cell Biol* **2**, 378-386 (2001).
- 803 41. S. F. Bakhoun *et al.*, Chromosomal instability drives metastasis through a cytosolic
804 DNA response. *Nature* **553**, 467-472 (2018).
- 805 42. S. A. Mookerjee, C. L. Quinlan, H. S. Wong, P. Dighe, M. D. Brand, Plate-Based
806 Measurement of Respiration by Isolated Mitochondria. *Methods Mol Biol* **1782**, 301-313
807 (2018).
- 808 43. L. B. Tanner *et al.*, Four Key Steps Control Glycolytic Flux in Mammalian Cells. *Cell*
809 *Syst* **7**, 49-62.e48 (2018).
- 810 44. R. J. DeBerardinis, N. S. Chandel, We need to talk about the Warburg effect. *Nat Metab*
811 **2**, 127-129 (2020).
- 812 45. C. Klijn *et al.*, A comprehensive transcriptional portrait of human cancer cell lines. *Nat*
813 *Biotechnol* **33**, 306-312 (2015).
- 814 46. D. P. Cook, B. C. Vanderhyden, Transcriptional census of epithelial-mesenchymal
815 plasticity in cancer. *Science Advances* **8**, eabi7640 (2022).
- 816 47. D. Ahmed, E. Cassol, Role of cellular metabolism in regulating type I interferon
817 responses: Implications for tumour immunology and treatment. *Cancer Letters* **409**, 20-
818 29 (2017).
- 819 48. J. D. Burke, L. C. Platanius, E. N. Fish, Beta interferon regulation of glucose metabolism
820 is PI3K/Akt dependent and important for antiviral activity against coxsackievirus B3. *J*
821 *Virol* **88**, 3485-3495 (2014).
- 822 49. B. Wang *et al.*, Glycolysis-dependent histone deacetylase 4 degradation regulates
823 inflammatory cytokine production. *Mol Biol Cell* **25**, 3300-3307 (2014).
- 824 50. H. Jiang *et al.*, PFKFB3-Driven Macrophage Glycolytic Metabolism Is a Crucial
825 Component of Innate Antiviral Defense. *J Immunol* **197**, 2880-2890 (2016).
- 826 51. T. Shirai *et al.*, The glycolytic enzyme PKM2 bridges metabolic and inflammatory
827 dysfunction in coronary artery disease. *J Exp Med* **213**, 337-354 (2016).
- 828 52. W. Zhang *et al.*, Lactate Is a Natural Suppressor of RLR Signaling by Targeting MAVS.
829 *Cell* **178**, 176-189.e115 (2019).
- 830 53. J. D. Rabinowitz, S. Enerbäck, Lactate: the ugly duckling of energy metabolism. *Nat*
831 *Metab* **2**, 566-571 (2020).
- 832 54. H. H. Lee *et al.*, Removal of N-Linked Glycosylation Enhances PD-L1 Detection and
833 Predicts Anti-PD-1/PD-L1 Therapeutic Efficacy. *Cancer Cell* **36**, 168-178.e164 (2019).

- 834 55. C.-W. Li *et al.*, Glycosylation and stabilization of programmed death ligand-1 suppresses
835 T-cell activity. *Nat Commun* **7**, 12632 (2016).
- 836 56. K. Kaira, I. Kuji, H. Kagamu, Value of 18F-FDG-PET to predict PD-L1 expression and
837 outcomes of PD-1 inhibition therapy in human cancers. *Cancer Imaging* **21**, 11 (2021).
- 838 57. J. Pacheco-Torres, M. F. Penet, Y. Mironchik, B. Krishnamachary, Z. M. Bhujwalla, The
839 PD-L1 metabolic interactome intersects with choline metabolism and inflammation.
840 *Cancer Metab* **9**, 10 (2021).
- 841 58. I. San-Millán, C. G. Julian, C. Matarazzo, J. Martinez, G. A. Brooks, Is Lactate an
842 Oncometabolite? Evidence Supporting a Role for Lactate in the Regulation of
843 Transcriptional Activity of Cancer-Related Genes in MCF7 Breast Cancer Cells.
844 *Frontiers in oncology* **9**, (2020).
- 845 59. R. Haas *et al.*, Lactate Regulates Metabolic and Pro-inflammatory Circuits in Control of
846 T Cell Migration and Effector Functions. *PLoS Biol* **13**, e1002202 (2015).
- 847 60. D. Zhang *et al.*, Metabolic regulation of gene expression by histone lactylation. *Nature*
848 **574**, 575-580 (2019).
- 849 61. Q. Xin *et al.*, Lactylation: a Passing Fad or the Future of Posttranslational Modification.
850 *Inflammation* **45**, 1419-1429 (2022).
- 851 62. M. C. Bourgeois-Daigneault *et al.*, Neoadjuvant oncolytic virotherapy before surgery
852 sensitizes triple-negative breast cancer to immune checkpoint therapy. *Science*
853 *translational medicine* **10**, (2018).
- 854 63. E. Panagioti *et al.*, Immunostimulatory bacterial antigen-armed oncolytic measles
855 virotherapy significantly increases the potency of anti-PD1 checkpoint therapy. *J Clin*
856 *Invest* **131**, (2021).
- 857 64. L. Young, J. Sung, G. Stacey, J. R. Masters, Detection of Mycoplasma in cell cultures.
858 *Nat Protoc* **5**, 929-934 (2010).
- 859 65. J. S. Diallo, M. Vähä-Koskela, F. Le Boeuf, J. Bell, Propagation, purification, and in vivo
860 testing of oncolytic vesicular stomatitis virus strains. *Methods Mol Biol* **797**, 127-140
861 (2012).
- 862 66. N. L. Bray, H. Pimentel, P. Melsted, L. Pachter, Near-optimal probabilistic RNA-seq
863 quantification. *Nat Biotechnol* **34**, 525-527 (2016).
- 864 67. H. Pimentel, N. L. Bray, S. Puente, P. Melsted, L. Pachter, Differential analysis of RNA-
865 seq incorporating quantification uncertainty. *Nature Methods* **14**, 687-690 (2017).
- 866 68. M. Schubert *et al.*, Perturbation-response genes reveal signaling footprints in cancer gene
867 expression. *Nat Commun* **9**, 20 (2018).
- 868 69. M. Foroutan *et al.*, Single sample scoring of molecular phenotypes. *BMC Bioinformatics*
869 **19**, 404 (2018).
- 870 70. W. Guo, L. Jiang, S. Bhasin, S. M. Khan, R. H. Swerdlow, DNA extraction procedures
871 meaningfully influence qPCR-based mtDNA copy number determination. *Mitochondrion*
872 **9**, 261-265 (2009).
- 873 71. A. Subramanian *et al.*, Gene set enrichment analysis: A knowledge-based approach for
874 interpreting genome-wide expression profiles. *Proceedings of the National Academy of*
875 *Sciences* **102**, 15545-15550 (2005).
- 876 72. A. Liberzon *et al.*, The Molecular Signatures Database (MSigDB) hallmark gene set
877 collection. *Cell Syst* **1**, 417-425 (2015).
- 878

879 **Acknowledgements**

880 We would like to thank: Dr. Tang and the uOttawa Flow Cytometry and Virometry Core Facility,
881 Mr. Ortiz and the OHRI Flow Cytometry Core Facility, Dr. Naz and the uOttawa Metabolomics
882 Core Facility (supported by the Terry Fox Foundation and uOttawa), Ms. Delic and the Global
883 Tissue Consent program at The Ottawa Hospital, the Ottawa Methods Centre at OHRI, the
884 uOttawa Pre-clinical Imaging Core (RRID:SCR_021832), the uOttawa Louise Pelletier Histology
885 Core Facility (RRID: SCR_021737), and the ACVS staff. Thank you to all former and current
886 Ardolino lab members for fruitful and enlightening discussions. We are also thankful to Dr. Roy
887 for honest and insightful comments on the manuscript.

888

889 **Funding:** M.A. is supported by Ride for Dad, CIHR, and CRS; J.J.H., C.F-M., and D.P.C. are
890 recipients of CIHR Frederick Banting and Charles Best Canada Graduate Scholarships Doctoral
891 Awards; J.A-H is the recipient of an OGS scholarship; A.H. is the recipient of a BioCanRx
892 scholarship; M.M. is the recipient of a CAAIF postdoctoral fellowship; A.B is the recipient of
893 OGS and a University of Ottawa Heart Institute Research Scholarship; M.M.P. is the recipient of
894 a Schulich Leader Scholarship, a uOttawa UROP scholarship, and a NSERC USRA; M.F.C. is the
895 recipient of a Taggart-Parkes Fellowship; J.C.B is supported by CIHR, CCSRI, PCC, and TFRI;
896 B.H.R is supported by CIHR, NSERC and CFI; R.C.A is supported by the Terry Fox Foundation;
897 L.A.S is supported by CCSRI; M-C.B-D is supported by CIHR.

898

899 **Author Contributions:** Conceptualization: J.J.H., M-C.B-D., and M.A.; Formal analysis: J.J.H.,
900 J.A-H., D.P.C., E.Y., A.B., S.F., M.P., C.F-M., M.F.C., B.H.R, and M-C.B-D; Funding
901 acquisition: J.C.B., M.E.H., B.H.R., R.C.A., B.C.V., L.A.S., M-C.B-D, and M.A.; Investigation:

902 J.J.H., J.A-H., A.H., D.P.C., C.T.D., M.M., E.Y., A.B., S.F., C.F-M., M.F.C., and M.P.;
903 Methodology: J.J.H, B.H.R., R.C.A., M.E.H., and M-C.B-D; Resources: J.C.B., M.E.H., B.H.R.,
904 R.C.A., B.C.V., L.A.S., and M-C.B-D; Supervision: J.C.B., M.E.H., B.H.R., R.C.A., B.C.V.,
905 L.A.S., M-C.B-D, and M.A.; Visualization: J.J.H and M.A.; Writing-original draft: J.J.H. and
906 M.A.; Writing-review and editing: all authors.

907

908 **Competing interests:** MA is a Scientific Advisory Board Member for Aakha Therapeutics and is
909 under a contract agreement to perform sponsored research with Actym Therapeutics and Dragonfly
910 Therapeutics. Neither consulting nor sponsored research is related to the present article.

911

912 **Data availability**

913 The transcriptomic data that support the findings of this study are openly available in GEO at
914 <https://www.ncbi.nlm.nih.gov/geo/query/acc.cgi?acc=GSE210884>, accession number
915 GSE210884. The metabolomic data that support the findings of this study will be deposited in the
916 National Metabolomics Data Repository (NMDR).

917

918 **FIGURES AND LEGENDS**

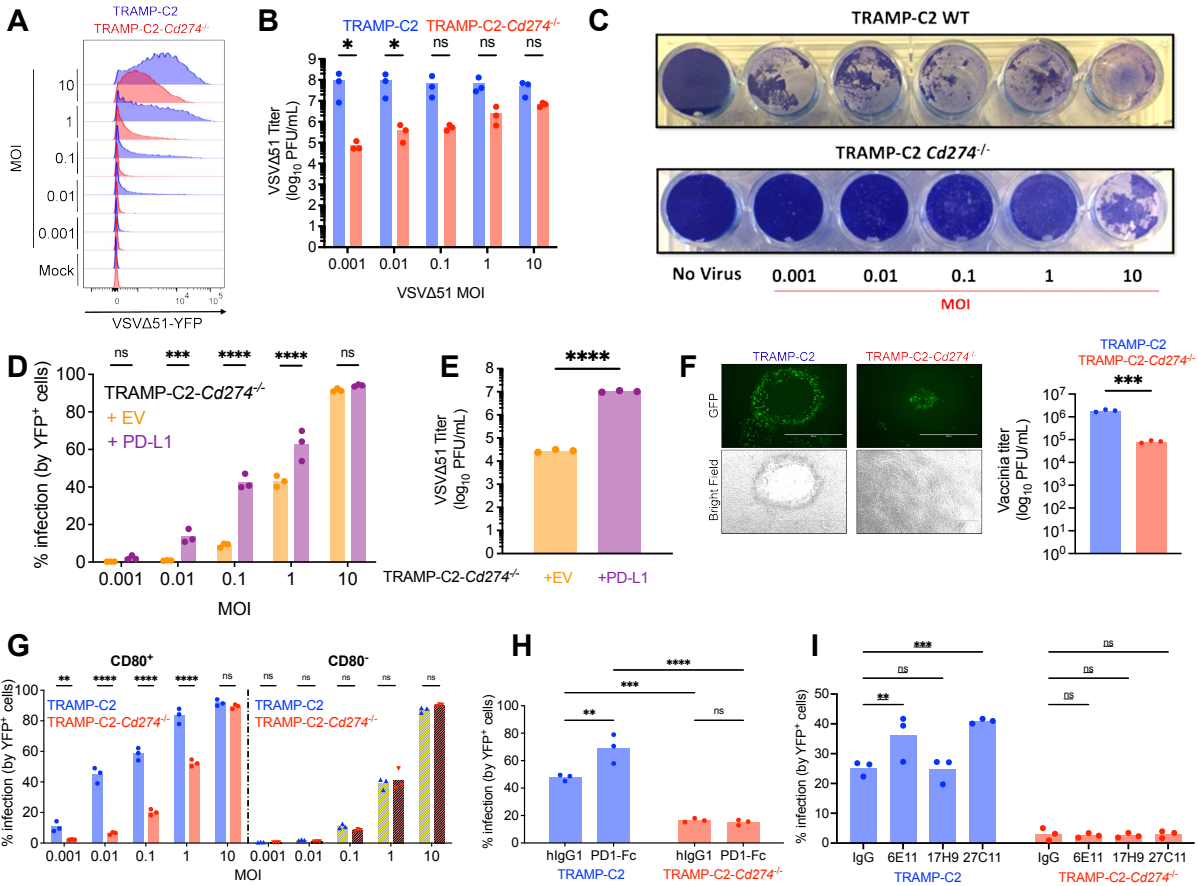


FIGURE 1

919

920 **Figure 1: PD-L1 engagement promotes OV infection.** (A-C) TRAMP-C2 and
 921 TRAMP-C2-*Cd274*^{-/-} cells were infected with VSVΔ51-YFP at indicated MOIs and subjected to
 922 flow cytometry to quantify the viral YFP reporter 24 hours post-infection (A), plaque assay to
 923 quantify viral titers 24 hours post-infection (B), or Coomassie staining to visualize cell death 48
 924 hours post-infection (C). The data depicted are representative of 4 experiments performed with
 925 similar results, n=3 biological replicates for the viral titer data. Statistical analysis by two-way
 926 ANOVA with Šidák's correction for multiple comparisons. (D-E) TRAMP-C2-*Cd274*^{-/-}
 927 transduced with PD-L1 or empty vector were infected with VSVΔ51-YFP at indicated MOIs for
 928 24 hours and analyzed by flow cytometry (D), or by plaque assay (E). The data depicted are
 929 representative of 3 performed with similar results. Statistical analysis by two-way ANOVA with

930 Šídák's correction for multiple comparisons in **D** and two-tailed unpaired Student's t-test in **E**. (**F**)
931 TRAMP-C2 cells were infected with GFP-expressing vaccinia virus (Copenhagen strain) at MOI
932 0.1 for 48 hours, prior to fluorescence imaging. Representative of two performed with similar
933 results. Viral titer was assessed by plaque assay, statistical analysis by two-tailed unpaired
934 Student's t-test (***: $p < 0.001$). (**G**) CD80⁺ and CD80⁻ cells were isolated by FACS and subjected
935 to VSVΔ51-YFP at indicated MOIs for 24 hours prior to flow cytometry to quantify viral YFP
936 reporter. The experiment depicted is representative of 3 performed with similar results. Statistical
937 analysis by two-way ANOVA with Šídák's correction for multiple comparisons. (**H**) TRAMP-C2
938 and TRAMP-C2-*Cd274*^{-/-} were pre-treated for 24 hours with 500 ng of recombinant PD-1-Fc
939 chimeric protein, and infected with VSVΔ51-YFP at MOI 0.1 for 24 hours prior to analysis by
940 flow cytometry. The experiment depicted is representative of 3 performed with similar results.
941 Statistical analysis by two-way ANOVA with Šídák's correction for multiple comparisons. (**I**)
942 TRAMP-C2 and TRAMP-C2-*Cd274*^{-/-} were pre-treated for 24 hours with 10 μg of PD-L1
943 antibodies, and infected with VSVΔ51-YFP at MOI 0.1 for 24 hours prior to analysis by flow
944 cytometry. The experiment depicted is representative of 3 performed with similar results.
945 Statistical analysis by two-way ANOVA with Šídák's correction for multiple comparisons.

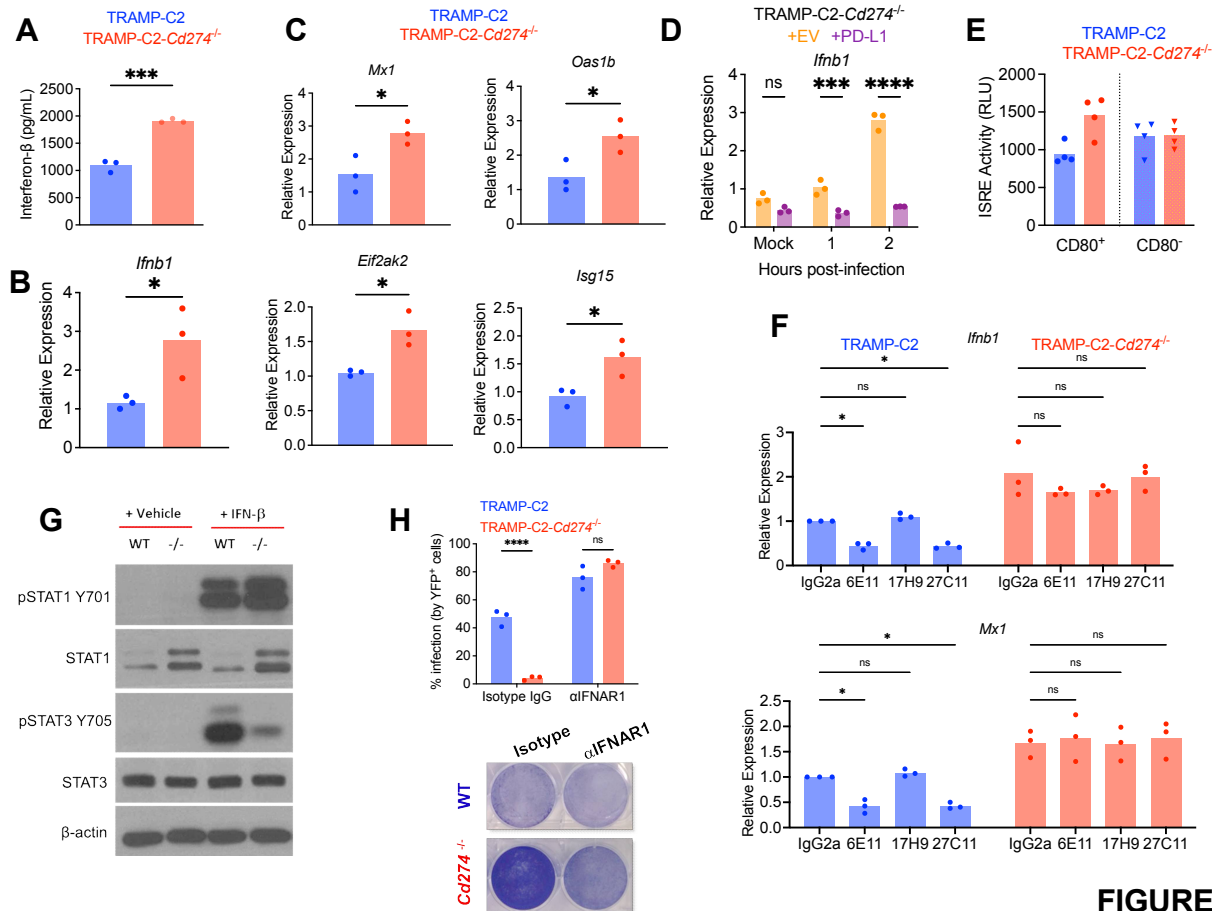


FIGURE 2

946

947 **Figure 2: PD-L1 inhibits the type I IFN response to OV.** (A-B) IFN-β protein in culture
 948 supernatant (by ELISA, A) or transcript levels (by qPCR, B) were quantified following infection
 949 with VSVΔ51-YFP for 8 hours. Statistical analysis with two-tailed unpaired Student's t-test. (C)
 950 Expression of ISGs was quantified following infection with VSVΔ51-YFP for 8 hours. Statistical
 951 analysis with two-tailed unpaired Student's t-test. (D) TRAMP-C2-Cd274^{-/-} transduced with
 952 PD-L1 or empty vector were infected with VSVΔ51-YFP at MOI 0.1 and analyzed by qPCR at
 953 indicated times post-infection to quantify *Ifnb1* transcripts. The data depicted are representative of
 954 3 performed with similar results. Statistical analysis by two-way ANOVA with Šidák's correction
 955 for multiple comparisons. (E) Type I IFN in culture supernatant was quantified using the
 956 L929-ISRE reporter cell line, in CD80⁺ and CD80⁻ cells isolated by FACS and infected with

957 VSVΔ51-YFP for 8 hours. The experiment depicted is representative of 3 performed with similar
958 results. Statistical analysis by one-way ANOVA with Šídák's correction for multiple comparisons.
959 (F) TRAMP-C2 and TRAMP-C2-*Cd274*^{-/-} were pre-treated for 24 hours with 5 μg of PD-L1
960 antibodies, and infected with VSVΔ51-YFP at MOI 0.1 for 8 hours prior to qPCR analysis. The
961 experiment depicted is representative of 3 performed with similar results. Statistical analysis by
962 two-way ANOVA with Šídák's correction for multiple comparisons. (G) TRAMP-C2 and
963 TRAMP-C2-*Cd274*^{-/-} cells were cultured in non-supplemented DMEM for 24 hours and treated
964 with 200 units of recombinant murine IFN-β for 10 minutes prior to analysis by western blotting.
965 The images depicted are representative of 3 performed with similar results. (H) TRAMP-C2 and
966 TRAMP-C2-*Cd274*^{-/-} were pre-treated with 25 μg of anti-IFNAR1 for 24 hours, followed by
967 infection with VSVΔ51-YFP at MOI 0.1 for 24 hours prior to analysis by Coomassie staining or
968 flow cytometry. The experiments depicted are representative of 3 performed with similar results.
969 Statistical analysis by two-way ANOVA with Šídák's correction for multiple comparisons.

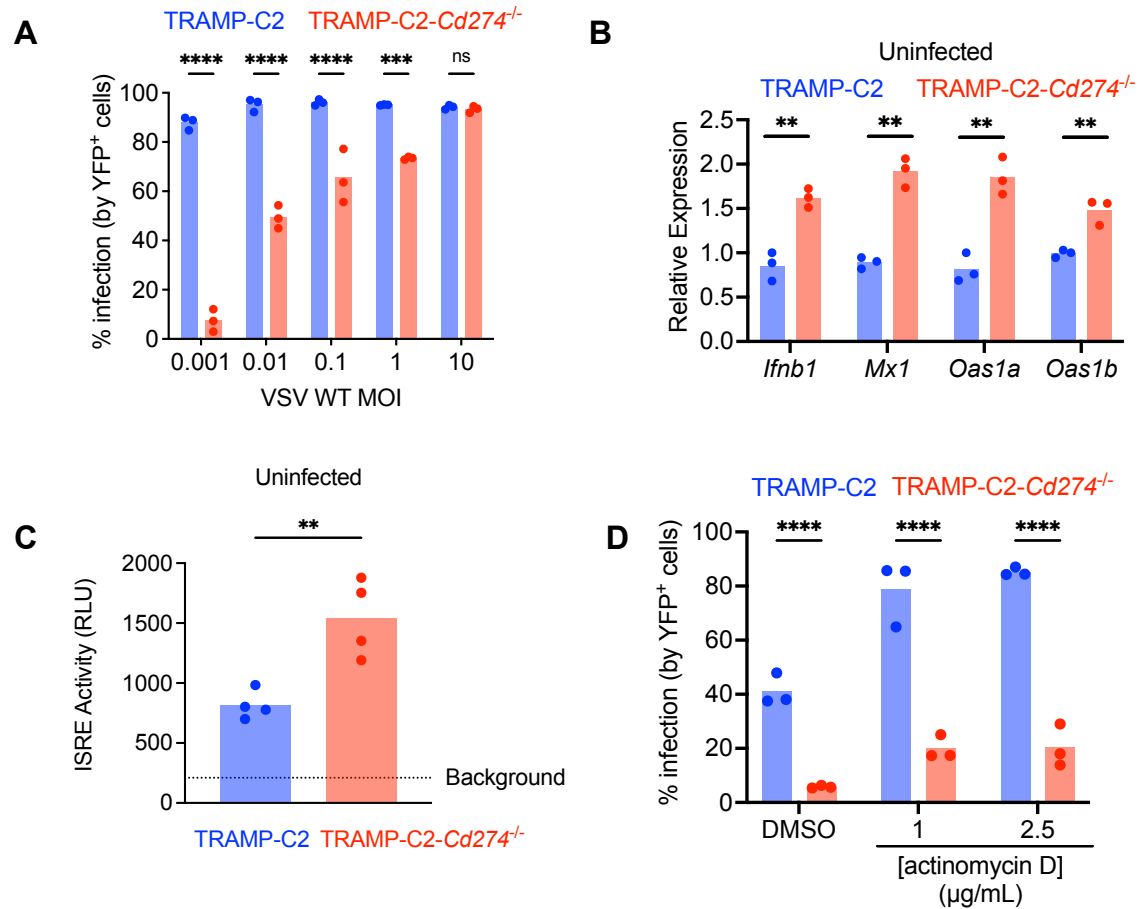


FIGURE 3

970

971 **Figure 3: PD-L1 poises cancer cells to be more sensitive to viral infection.** (A) TRAMP-C2

972 and TRAMP-C2-*Cd274*^{-/-} cells were infected with VSV WT at indicated MOIs for 24 hours prior

973 to analysis by plaque assay. The experiment depicted is representative of 3 performed with similar

974 results. Statistical analysis by two-way ANOVA with Šídák's correction for multiple comparisons.

975 (B) qPCR analysis of type I IFN and ISG transcripts expressed by TRAMP-C2 and

976 TRAMP-C2-*Cd274*^{-/-} cells prior to infection. Statistical analysis by two-way ANOVA with Šídák's

977 correction for multiple comparisons. (C) Measurement of type I IFN in uninfected TRAMP-C2

978 and TRAMP-C2-*Cd274*^{-/-} supernatant using the L929-ISRE reporter line. The experiment depicted

979 is representative of 3 performed with similar results. Statistical analysis by two-tailed unpaired

980 Student's t-test. (D) TRAMP-C2 and TRAMP-C2-*Cd274*^{-/-} cells were infected with VSVΔ51-YFP

981 at MOI 0.1 and treated with actinomycin D (or DMSO as vehicle control) at the time of infection.
982 24 hours later, cells were analyzed by flow cytometry. The experiment depicted is representative
983 of 3 performed with similar results. Statistical analysis by two-way ANOVA with Šídák's
984 correction for multiple comparisons.
985

986

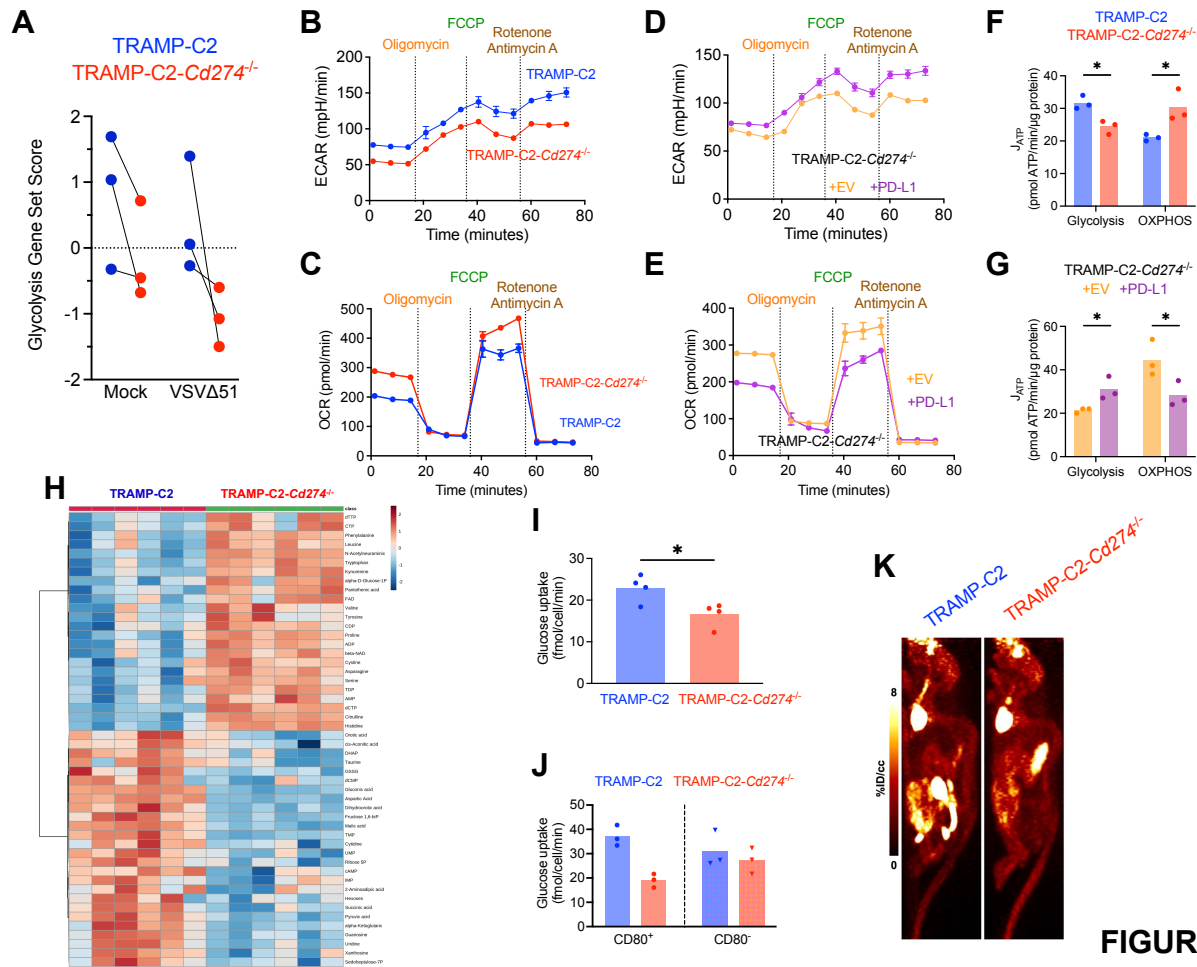


FIGURE 4

987

988 **Figure 4: PD-L1 promotes Warburg metabolism in TRAMP-C2 cells.** (A) Scoring for
 989 expression of genes included in the glycolysis gene set. RNA-seq dataset performed on
 990 TRAMP-C2 and TRAMP-C2-Cd274^{-/-} either mock-infected or infected with VSVΔ51-YFP at
 991 MOI 0.1 for 8 hours (3 biological replicates per condition). (B-E) Seahorse metabolic flux analysis
 992 on TRAMP-C2, TRAMP-C2-Cd274^{-/-}, TRAMP-C2-Cd274^{-/-} + EV, and TRAMP-C2-Cd274^{-/-} +
 993 PD-L1 (tested in n=6 technical replicates). Extracellular acidification rate (ECAR) and oxygen
 994 consumption rate (OCR) are measures of glycolysis and mitochondrial respiration, respectively.
 995 Images depicted are representative of 3 experiments with similar results. (F-G) Bioenergetic
 996 calculations based on Seahorse metabolic flux assay. N=3 biological replicates. (H) Hierarchical

997 clustered heat map depicting relative abundance of 50 metabolites quantified in untargeted
998 metabolomics of TRAMP-C2 and TRAMP-C2-*Cd274*^{-/-} cells. 6 biological replicates per cell line
999 are shown. **(I-J)** Glucose uptake was measured in TRAMP-C2 and TRAMP-C2-*Cd274*^{-/-} cells (I),
1000 as well as CD80⁺ vs CD80⁻ cells FACS-isolated from TRAMP-C2 or TRAMP-C2-*Cd274*^{-/-} cells
1001 (J). The experiments depicted are representative of 3 performed with similar results. Statistical
1002 analysis by two-way ANOVA with Šídák's correction for multiple comparisons. **(K)** Male NCG
1003 mice were implanted with subcutaneous TRAMP-C2 or TRAMP-C2-*Cd274*^{-/-} tumors.
1004 Standardized uptake value (SUV) of [¹⁸F]-fluorodeoxyglucose was assessed by PET imaging. The
1005 two mice shown are representative of 5-6 analyzed.
1006

1007

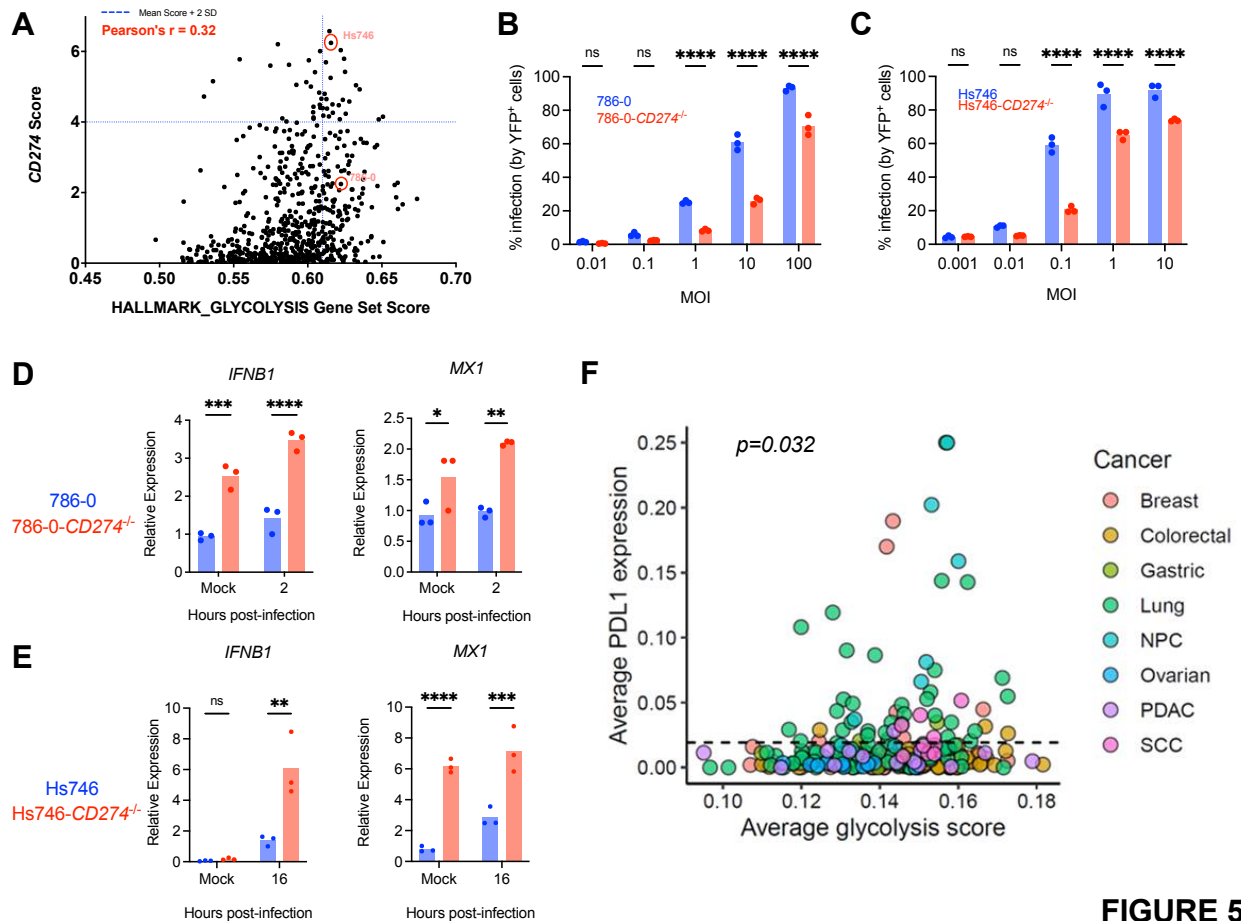


FIGURE 5

1008

1009 **Figure 5: PD-L1 inhibits type I IFN responses in human cancer cells.** (A) Bioinformatic
 1010 analysis of publicly available RNA-seq from 675 human cancer cell lines, scored for their
 1011 expression of PD-L1 (*CD274*) and glycolysis gene signatures. Blue lines on plot indicate mean +
 1012 2 SD; Pearson correlation coefficient is indicated. (B and C) 786-0 and Hs746 (WT and *CD274*^{-/-})
 1013 infected with VSVΔ51-YFP at indicated MOIs for 24 hours prior to analysis by flow cytometry.
 1014 Experiments depicted are representative of 3 performed with similar results. Statistical analysis by
 1015 two-way ANOVA with Šidák's correction for multiple comparisons. (D-E) 786-0 and
 1016 786-0-*CD274*^{-/-} cells (D) or Hs746 and Hs746-*CD274*^{-/-} cells (E) infected with VSVΔ51-YFP at
 1017 MOI 1 or 0.1, respectively (or mock-infected) prior to qPCR analysis for *IFNB1* and *MX1*

1018 transcripts. n=3 biological replicates. Statistical analysis by two-way ANOVA with Šídák's
1019 correction for multiple comparisons. *: p<0.05; **: p<0.01; ***: p<0.001; ****: p<0.0001. (F)
1020 Association between the expression of PD-L1 and *Glycolysis*-associated genes in the malignant
1021 cells of 266 tumours. Each point represents the average profile of malignant cells from scRNA-seq
1022 data sets, and dotted line represents mean PD-L1 expression of samples. Expression values reflect
1023 log-transformed gene counts per 10k transcripts and *Glycolysis* activity represents gene set scores
1024 from the associated MSigDB Hallmark gene set. Statistical significance assessed by Wilcoxon
1025 rank-sum test to compare glycolysis scores of tumors expressing PD-L1 above or below mean
1026 expression. NPC: nasopharyngeal cancer, PDAC: pancreatic ductal adenocarcinoma, SCC:
1027 squamous cell carcinoma.
1028

1029

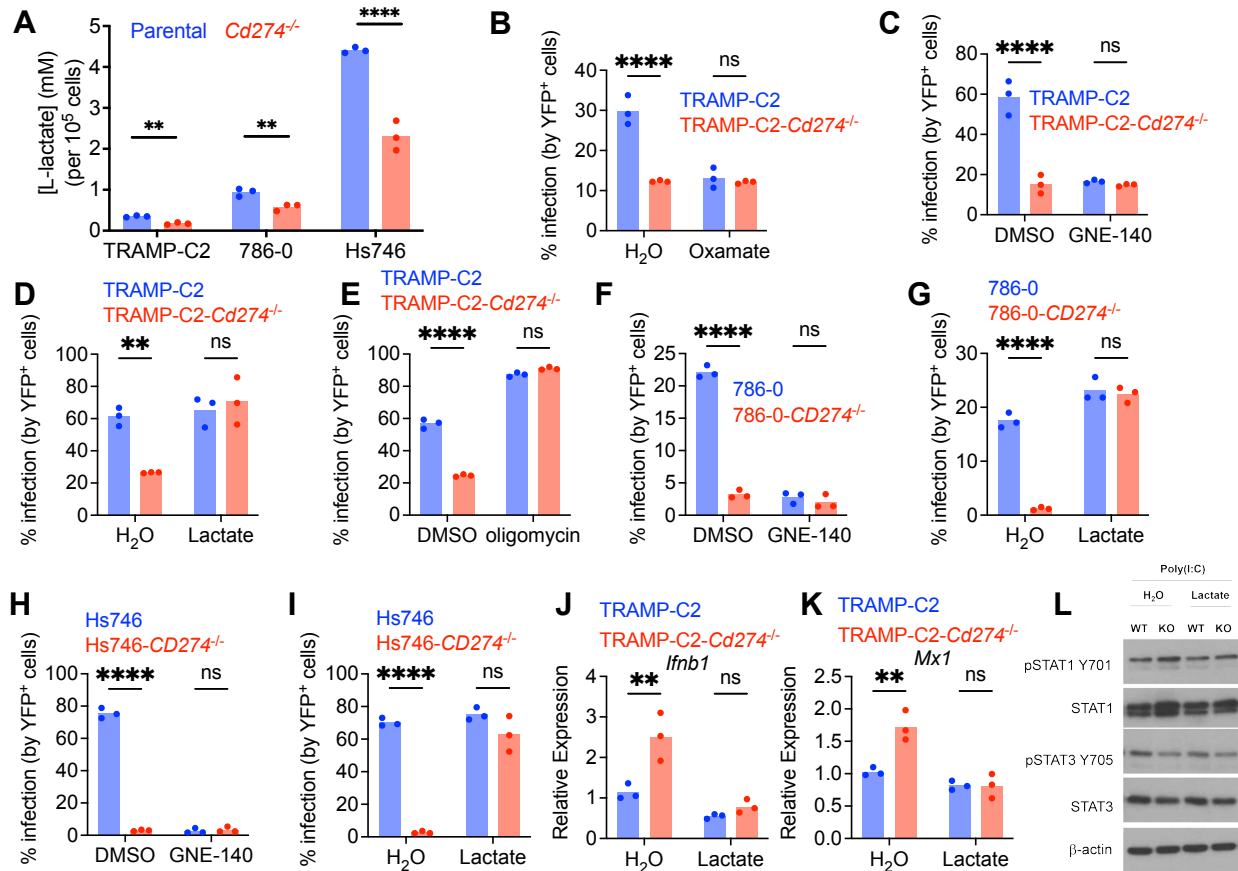


FIGURE 6

1030

1031 **Figure 6: PD-L1 inhibits type I IFN via lactate dynamics.**

1032 (A) Lactate quantification in TRAMP-C2, 786-0 or Hs746 culture supernatant. n=3 biological
1033 replicates. Statistical analysis by two-tailed unpaired Student's t-test. *:p<0.05; ***: p<0.001

1034 (B-E) TRAMP-C2 and TRAMP-C2-*Cd274*^{-/-} cells were pre-treated with oxamate at 10 mM (B);
1035 GNE-140 at 10 μM (C); lactate at 5 mM (D); oligomycin at 0.2 μM (E) for 24 hours, followed by
1036 infection with VSVΔ51-YFP at MOI 0.1 for 24 hours prior to analysis by flow cytometry.

1037 Experiments depicted are representative of 3 performed with similar results. Statistical analysis by
1038 two-way ANOVA with Šídák's correction for multiple comparisons. (F-G) 786-0 and 786-0-

1039 *CD274*^{-/-} cells were pre-treated with GNE-140 at 10 μM (F) or lactate at 5 mM (G) for 24 hours,

1040 followed by infection with VSV Δ 51-YFP at MOI 1 for 24 hours prior to analysis by flow
1041 cytometry. Experiments depicted are representative of 3 performed with similar results. Statistical
1042 analysis by two-way ANOVA with Šídák's correction for multiple comparisons. **(H-I)** Hs746 and
1043 Hs746-*CD274*^{-/-} cells were pre-treated with GNE-140 at 10 μ M (H) or lactate at 5 mM (I) for 24
1044 hours, followed by infection with VSV Δ 51-YFP at MOI 0.1 for 24 hours prior to analysis by flow
1045 cytometry. Experiments depicted are representative of 3 performed with similar results. Statistical
1046 analysis by two-way ANOVA with Šídák's correction for multiple comparisons. **(J-K)**
1047 TRAMP-C2 and TRAMP-C2-*Cd274*^{-/-} cells were pre-treated with lactate at 5 mM for 24 hours,
1048 followed by infection with VSV Δ 51-YFP at MOI 0.1 for 8 hours prior to qPCR analysis for *Ifnb1*
1049 and *Mx1*. n=3 biological replicates. Statistical analysis by two-way ANOVA with Šídák's
1050 correction for multiple comparisons. **(L)** TRAMP-C2 and TRAMP-C2-*Cd274*^{-/-} cells were
1051 pre-treated with lactate at 5 mM for 24 hours, followed by transfection with poly(I:C) for 6 hours
1052 prior to western blotting analysis. Images depicted are representative of 3 with similar results.

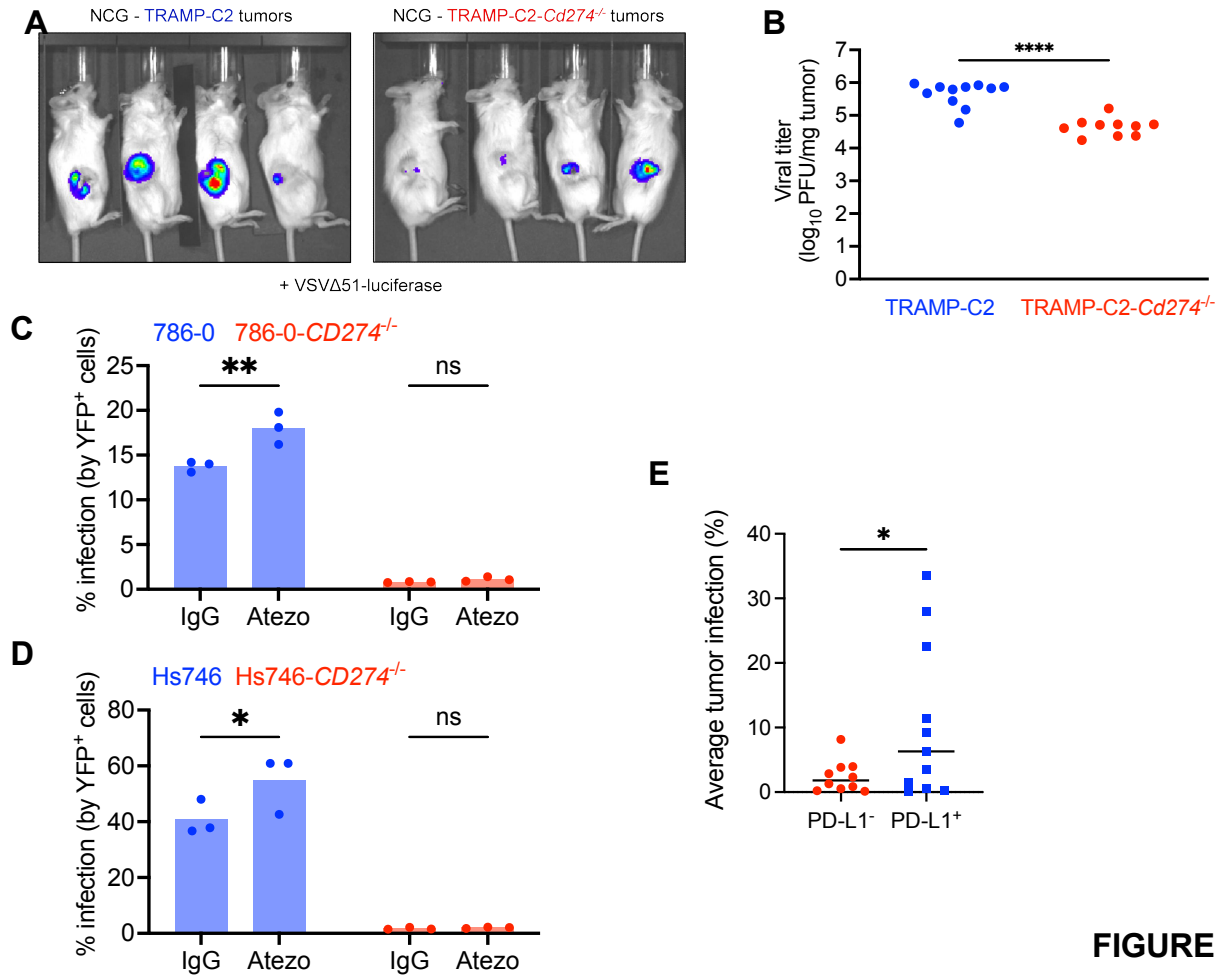


FIGURE 7

1053

1054 **Figure 7: PD-L1 promotes OV infection in vivo.** (A-B) Male NCG mice were implanted with
1055 subcutaneous TRAMP-C2 or TRAMP-C2-*Cd274*^{-/-} cells, and injected intra-tumoral with 10⁸ PFU
1056 of VSVΔ51 expressing a luciferase reporter. 24 hours post-infection, mice were injected subjected
1057 to bioluminescence imaging, and tumors were homogenized to quantify viral titers by plaque
1058 assay. The bioluminescence images are representative of 2 experiments with similar results.
1059 Statistical analysis by unpaired two-tailed Student's t-test. ****:p<0.0001. (C-D) 786-0 (C) and
1060 Hs746 (D) cells were treated with 5 μg of atezolizumab for 24 hours prior to VSVΔ51-YFP
1061 infection at MOI 1 or 0.1, respectively. 24 hours post-infection, cells were analyzed by flow
1062 cytometry to quantify the viral YFP reporter. Experiments depicted are representative of 3

1063 performed with similar results. Statistical analysis by two-way ANOVA with Šídák's correction
1064 for multiple comparisons. (E) PD-L1 tumor status (where PD-L1⁺ tumors are defined as >1%
1065 PD-L1⁺ tumor/immune cells) plotted against average tumor infection (percentage of tumor explant
1066 area that is YFP⁺). Statistical analysis by two-tailed unpaired Student's t-test. *:p<0.05

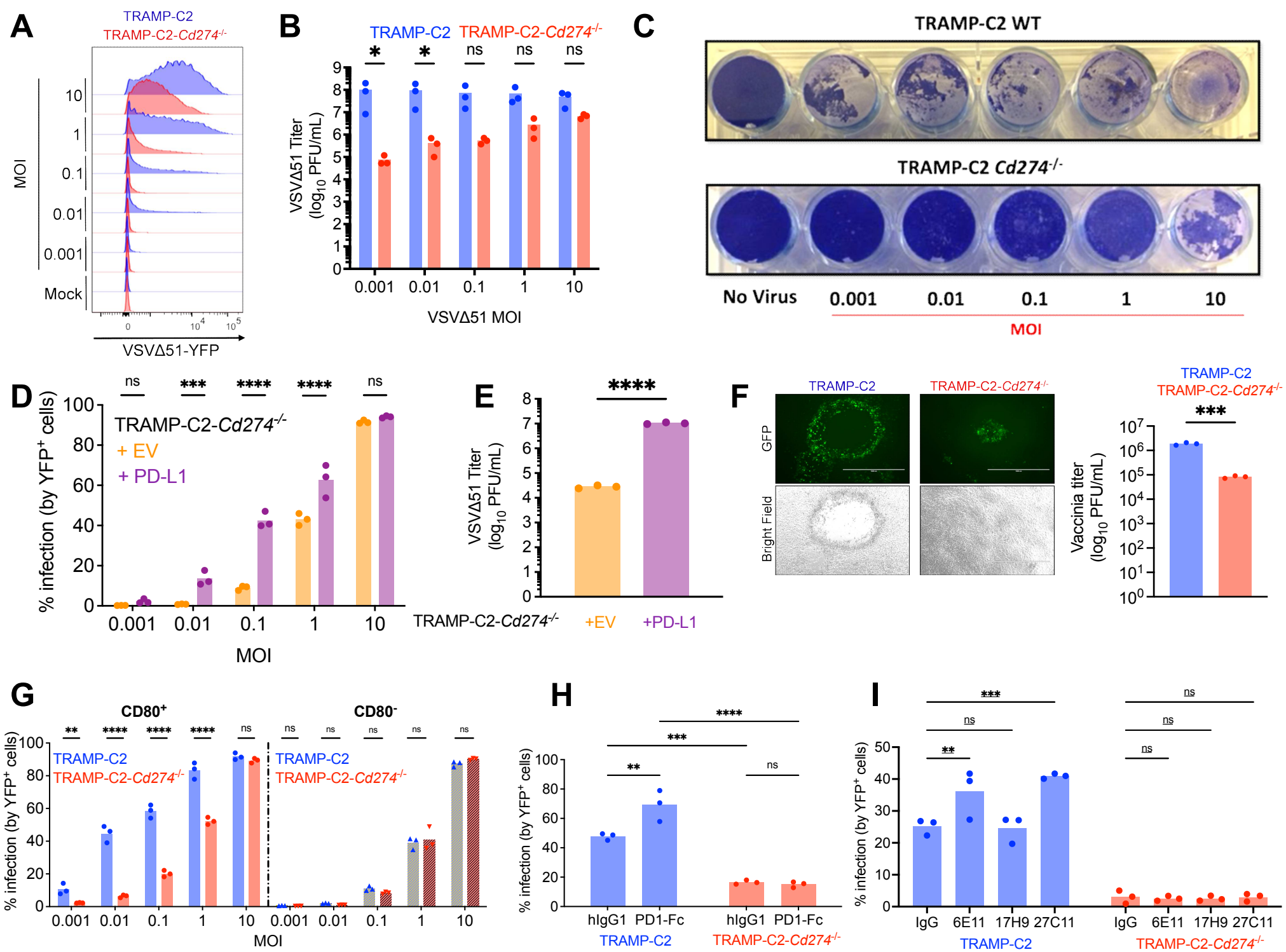


FIGURE 1

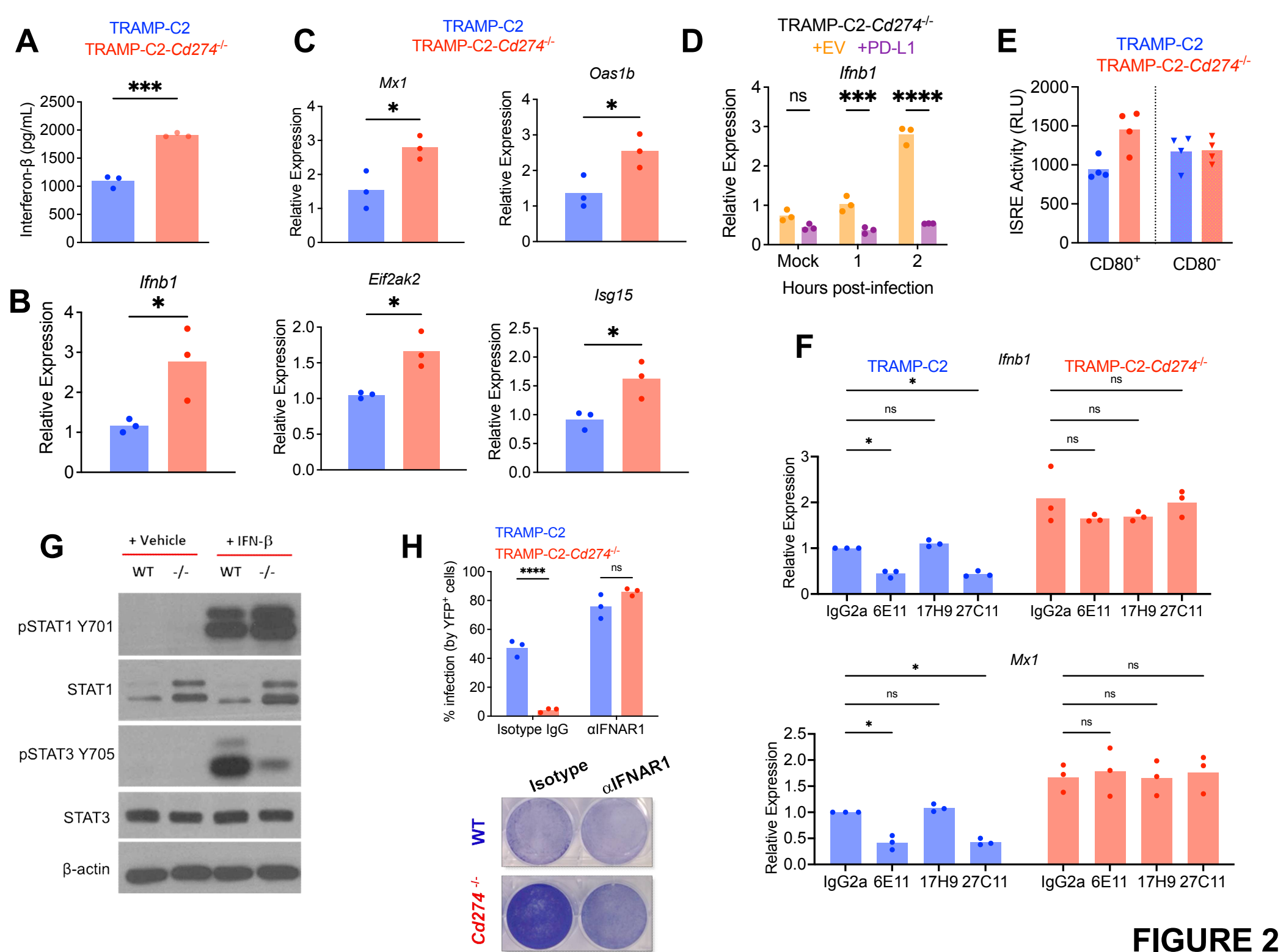
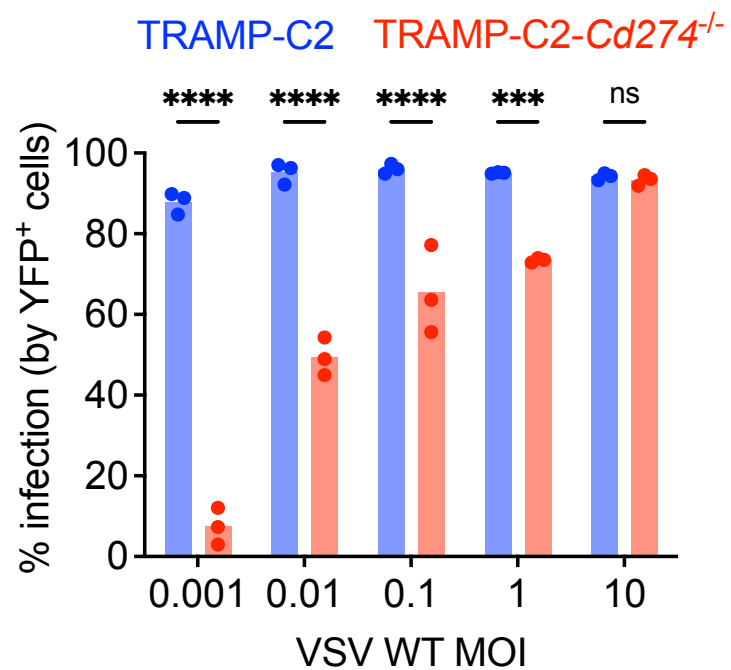
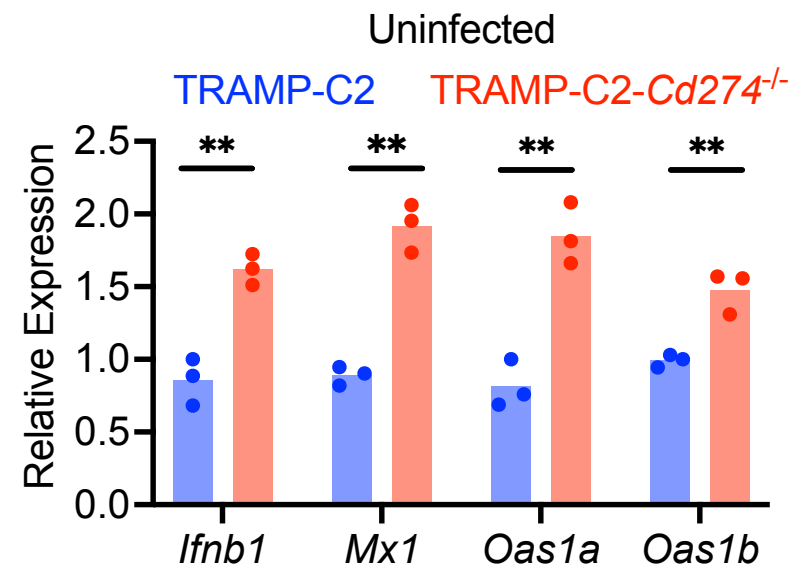
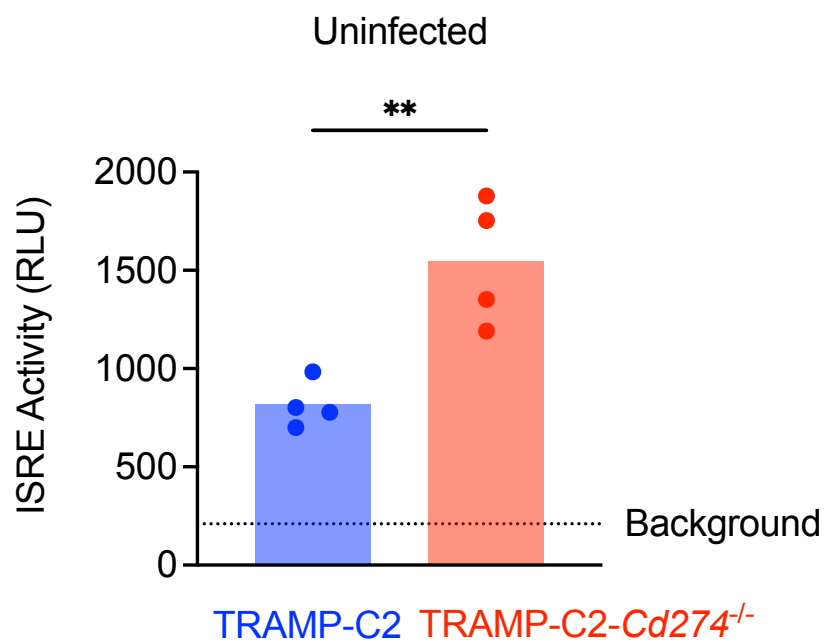
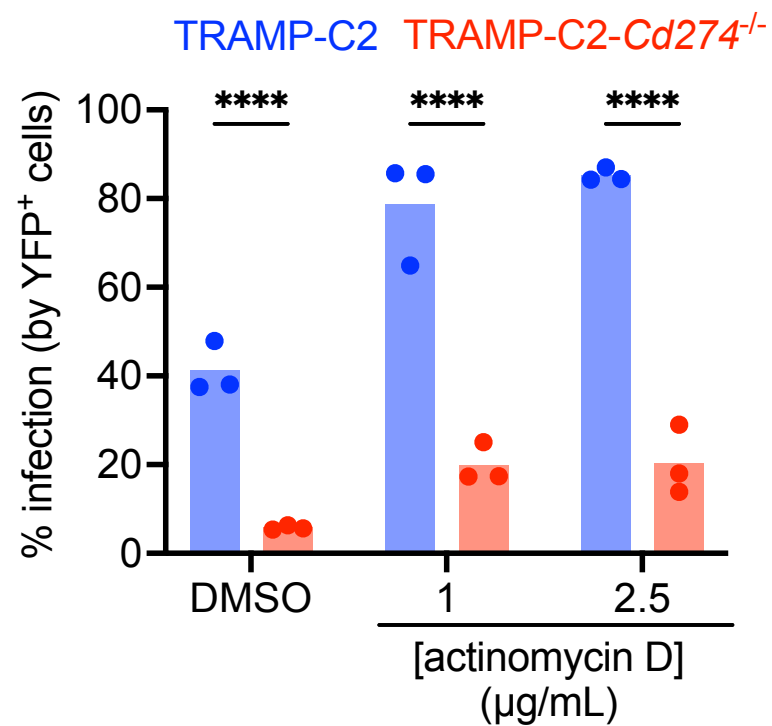
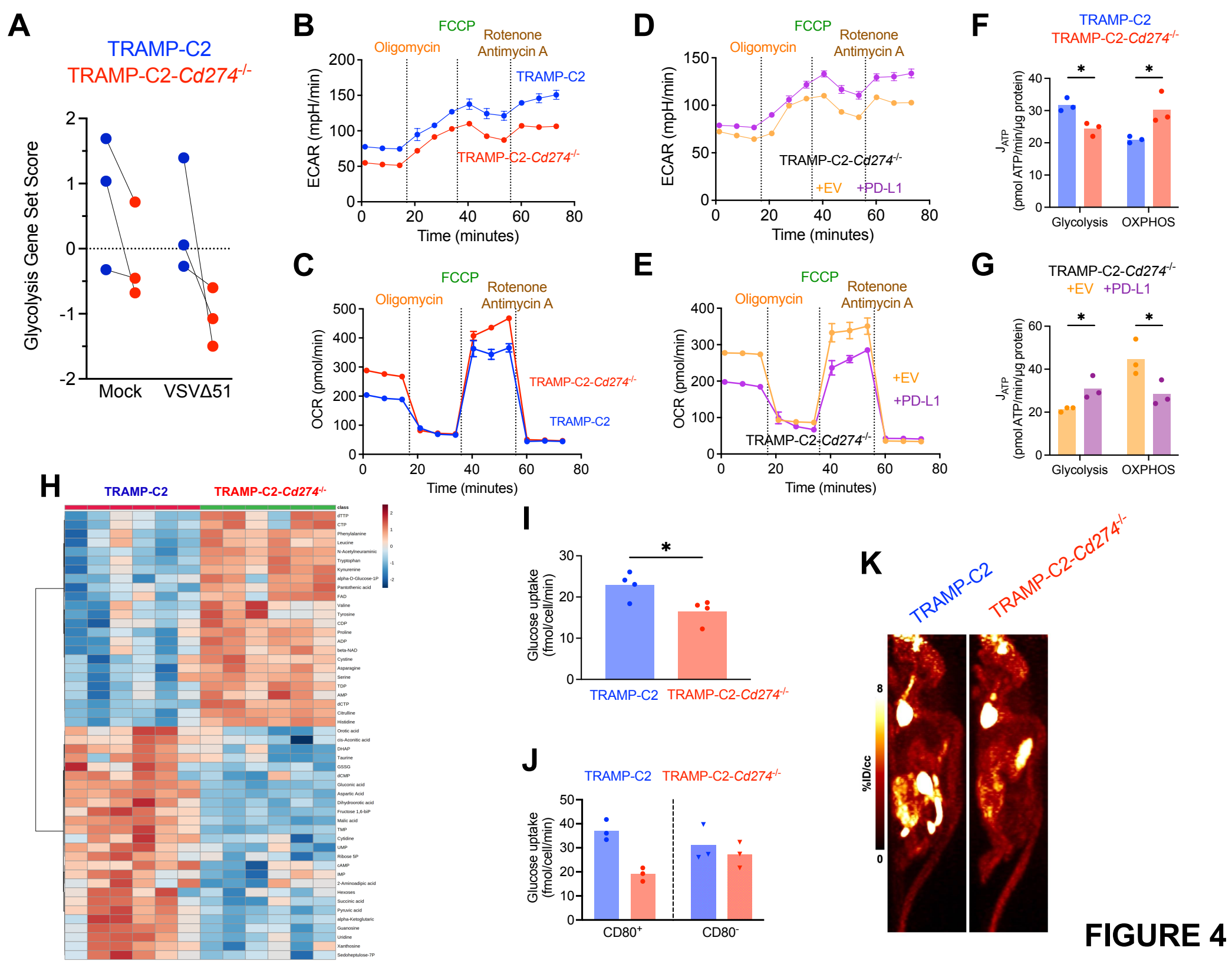


FIGURE 2

A**B****C****D****FIGURE 3**



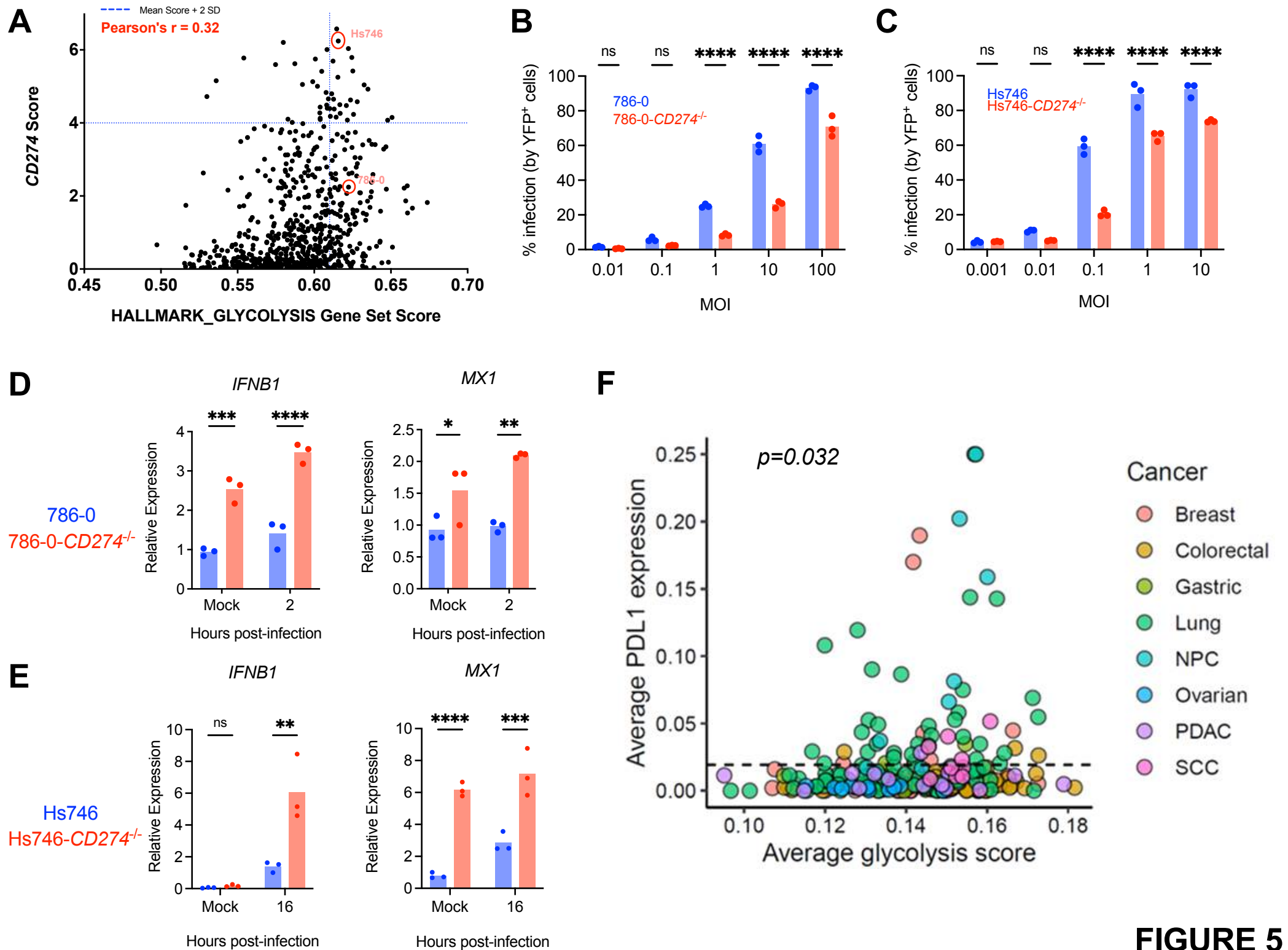


FIGURE 5

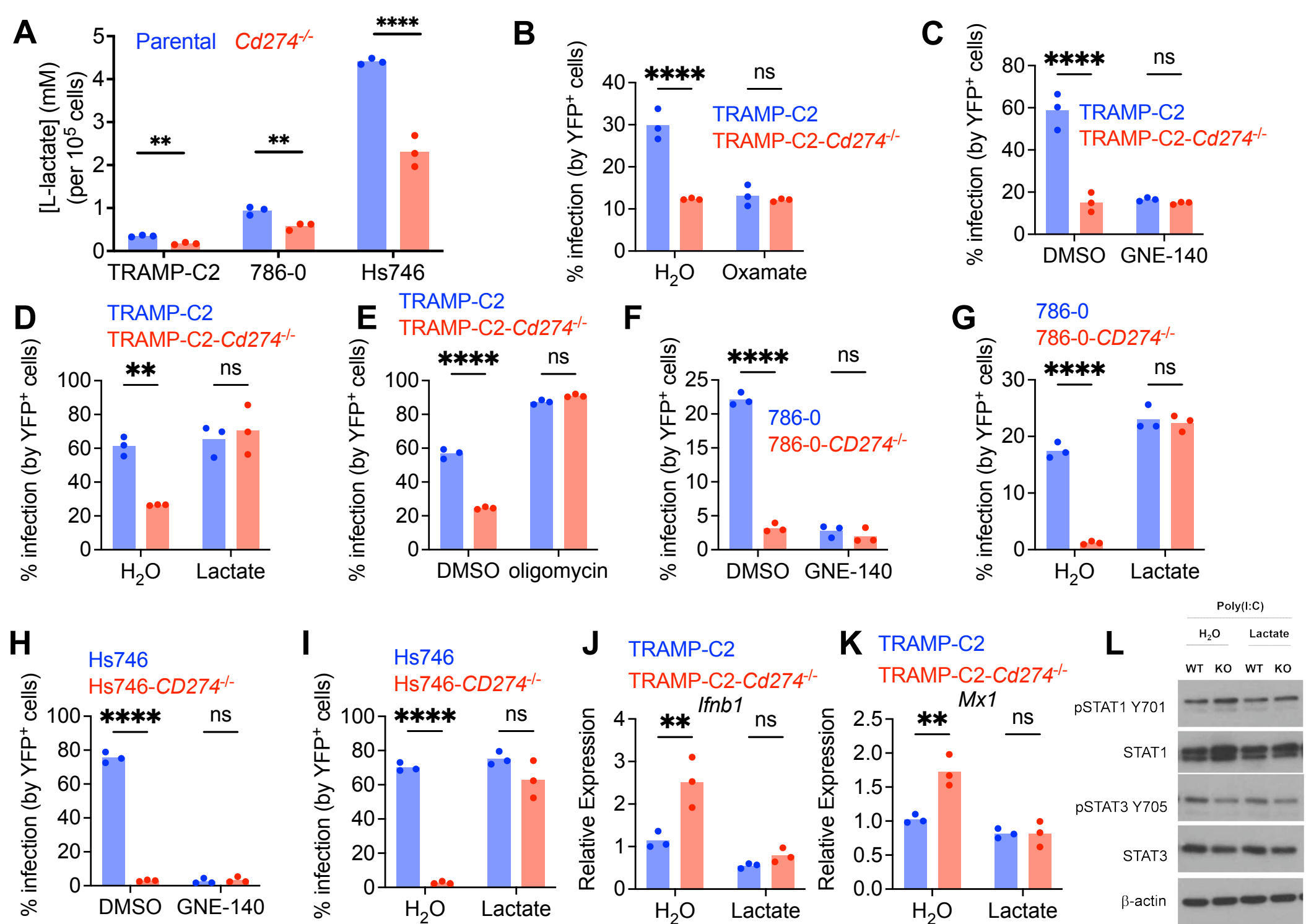


FIGURE 6

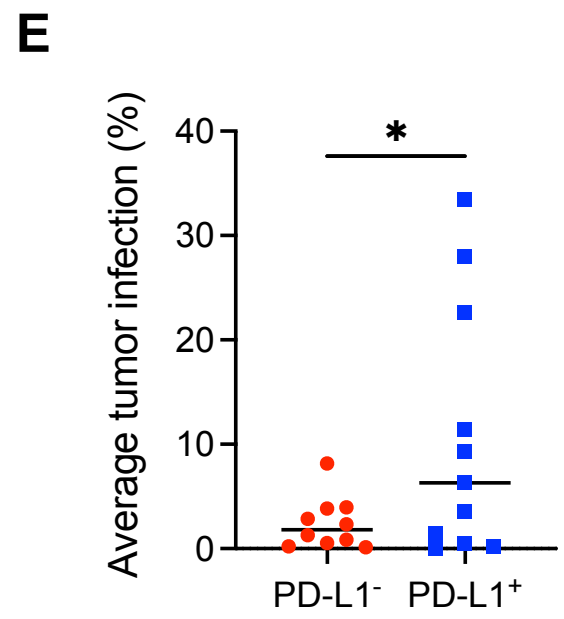
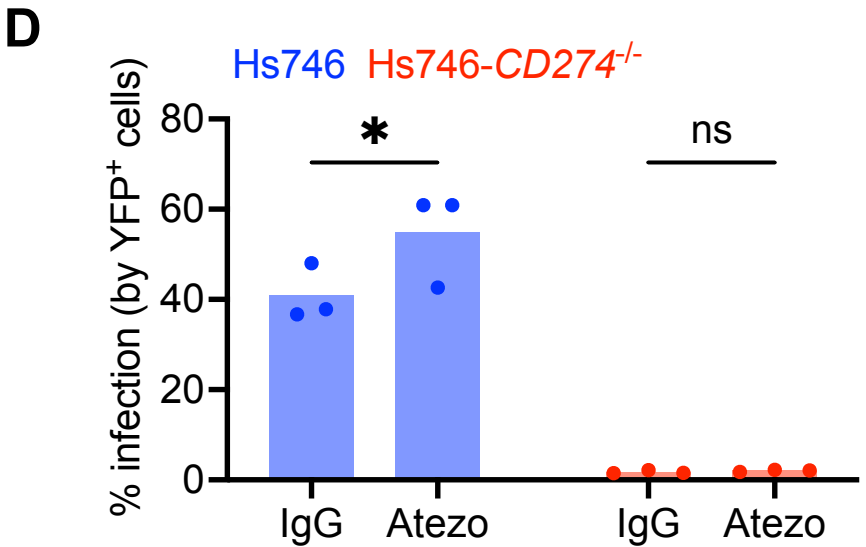
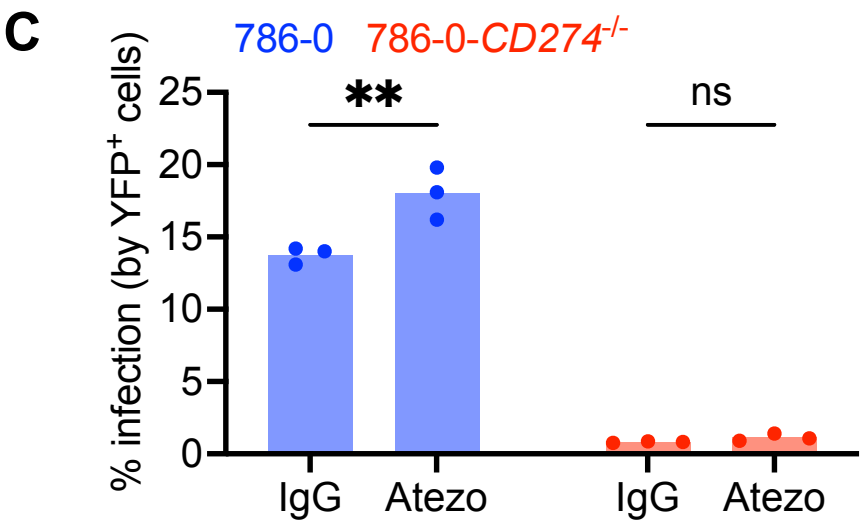
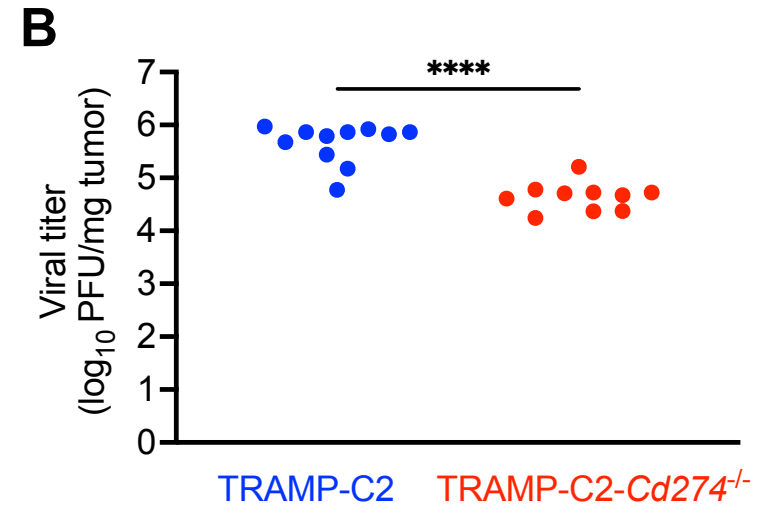
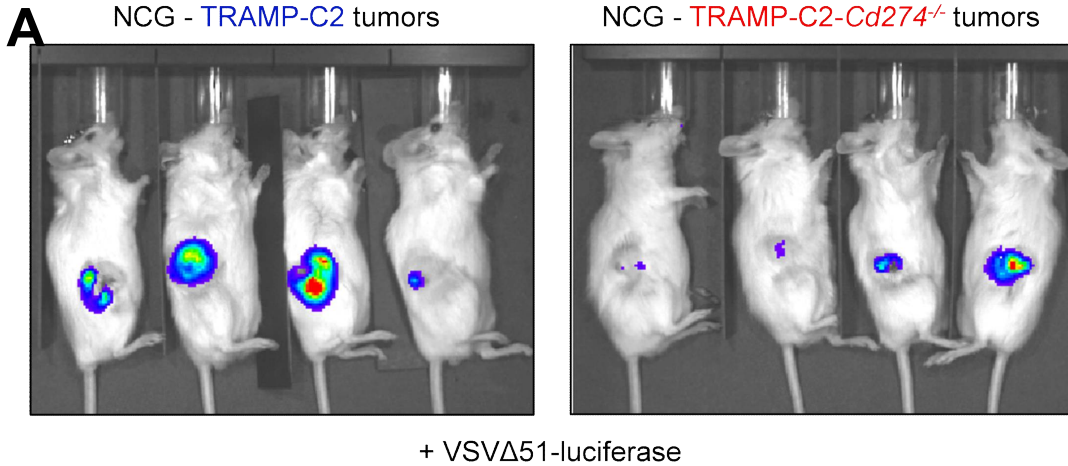


FIGURE 7